



Detailed Analysis of Variables Affecting Wing Kinematics of Bat Flight

Gaurav Bindal and Sparsh Sharma
Vellore Institute of Technology

Frank Janser and Eugen Neu
Fachhochschule Aachen

ABSTRACT

Body motions of flying animals can be very complex, especially when the body parts are greatly flexible and they interact with the surrounding fluid. The wing kinematics of an animal flight is governed by a large number of variables and thus the measurement of complete flapping flight is not so simple, making it very complex to understand the contribution of each parameter to the performance and hence, to decide the important parameters for constructing the kinematic model of a bat is nearly impossible. In this paper, the influence of each parameter is uncovered and the variables that a specified reconstruction of bat flight should include in order to maximally reconstruct actual dimensional complexity, have been presented in detail. The effects of the different kinematic parameters on the lift coefficient are being resulted. The computation analysis of the lift coefficient for different camber thicknesses and various wing areas is done by unsteady thin airfoil theory and vortex lattice method, respectively.

CITATION: Bindal, G., Sharma, S., Janser, F., and Neu, E., "Detailed Analysis of Variables Affecting Wing Kinematics of Bat Flight," *SAE Int. J. Aerosp.* 6(2):2013, doi:10.4271/2013-01-9003.

INTRODUCTION

Since the dawn of the era, humans have always been fascinated and inspired by the movement of animals through the air. The animal flight has not only aroused passion but also served the most utilitarian function of inspiring design innovations. Nonetheless, the early attempts to develop a flapping wing MAV were bound to fail due to insufficient knowledge of the flapping motion and lack of tools required for the analyses and design of the unsteady flight, and consequently, research concerning flapping flight has been overshadowed by the study of fixed and rotary wing aircrafts for almost 100 years [1]. Interests in bio-inspired flight and rigorous desire to develop highly efficient and maneuverable flapping wing MAVs have resurfaced among the biologists and engineers in the last two decades. The greatly improved capabilities of modern equipments to image animal motion and visualize complex fluid flows have brought the attention back to animal flight research.

Although the tools for the analysis and design of vehicles optimized for steady flight are well developed, the mechanics of highly unsteady flight remains uncertain due to the gap

present in our understanding of the basic mechanics of the highly unsteady, three-dimensional and complex character of animal flight. This is an issue of growing interest, driven by the desire to build vehicles that can perform extremely unsteady aerodynamic maneuvers.

Flapping flight is the single most evolutionarily successful mode of animal locomotion: there are today over 1200 species of bats, more than 10 000 living species of flying birds, and somewhere between millions and tens of millions of species of flying insects [2]. Birds, insects and bats apply a variety of flapping patterns in hovering and forward flight to generate lift and thrust but among these, bats are proven to be the most superior and efficient flyers due to their highly articulated motion. Birds and insects can fold and rotate their wings but more than two dozen independently controlled joints overlaid in the flexible wing membrane [2, 3, 4] and highly deformable bones [5,6] enable the bat to fly at either positive or negative angle of attack, dynamically change wing camber and create complex 3D wing topology to achieve extraordinary flight performance. The difference in the wing kinematics of the bats with respect to birds and insects is irrespective of the flight speed and other flight conditions.

Bat wing kinematics is a very complex phenomenon (especially at slow flight speeds) with the wing changing its shape continuously as it flaps [7]. It cannot be simply viewed as a flapping plate, or even as a flapping plate with one or two simple hinges [1]. Many of the joints of the handwing are extended during the downstroke until the lower reversal point, where they begin to flex, and the wingtip moves closer to the body in horizontal direction. At the same time, early in the upstroke, the wingtip moves simultaneously upwards and outwards and the wing adapts an extended posture at the end of the upstroke. Moreover, the motion of the wingtip is not primarily vertical with respect to either gravity or the animal's body, and a strong wing tip vortex is shed from the wing tip during the downstroke and either from the wing tip or a more proximal joint during the upstroke. The wings sweep forward during downstroke, increasing the relative forward velocity, and sweep backward during upstroke alongwith decreasing the angle of attack. Moreover, adding to the complexity of the bat flight, the flight speed and elevation are not constant, but oscillate in synchrony with both the horizontal and vertical movements of the wing.

A bat's wing motion is not governed by one or two variables; instead the wing kinematics is a function of numerous variables, having a significant role in the wing kinematics. The kinematic measurements of such complex motions are very difficult due to the large number of variables involved and thus the contribution of each parameter to performance is not clearly apparent. In this study, the influence of all variables on wing kinematics has been uncovered in detail and priority variables (having the most significant influence on performance) are decided to be focused on for developing a kinematic model of the bat.

The flight of bats, much like that of birds has often been modeled to first approximation as quasi-steady, with wings treated as rigid plates [8, 9, 10]. The assumption of steady flight was largely necessitated by the lack of analytical and experimental tools to analyze the complex flows, but this situation has changed considerably in the past few years. Recently, numerous experiments on bats have been done by many scientists and engineers to study the importance of various parameters of the bat wing kinematics. In 2006, Tian [2] experimented and analyzed the bat flight kinematics and observed that bats possess unique flight characteristics at relatively low flight speeds, including a flexion of the wing during upstroke. Riskin [7], in 2008, used proper orthogonal decomposition method (POD) for assigning importance to kinematic variables, using dimensional complexity metric, concluding that it does not change with flight speeds. While in 2010, Riskin [11], Hubel [12] and Leigh [13] performed different studies on bats to analyze the variation in their wing posture and kinematics on account of varying body mass, flight speed and power output required, respectively. Leigh [13] found out that variation of kinematics alone can increase sufficient aerodynamic power to accommodate even a 21% increase in body weight. In 2012, Riskin [14] analyzed kinematics of the folding and unfolding of the bat wing

during upstroke motion for inertial cost of flight, while Rhea [15] studied the three-dimensional wingbeat kinematics of a bat to determine how factors affecting the lift production vary across flight speed and within wingbeat.

This paper explains the influence and importance of different variables on the wing shape and kinematics of a bat flight. The focus has been given on parameters which are critically important for the construction of the kinematic model of bat flight in order to maximally reconstruct actual dimensional complexity.

EFFECT OF PARAMETERS ON WING KINEMATICS

Bat wings have a high potential to adjust wing morphology according to the aerodynamic demands due to their highly flexible wings with flexible wing bones and a compliant wing membrane, enabling them to carefully control their wing shape and motion. The morphology and kinematics of a bat wing determines the resulting aerodynamic lift through the regulation of the flight speed, wing area and lift coefficient. Thrust and weight support of the bat is generated by the aerodynamic lift (L) of the wing, which is determined by the density of the medium (ρ), the speed of the wing relative to the air (U_{eff}), the wing area (S) and the lift coefficient (C_l) given by equation (1) [16]:

$$L = \frac{1}{2} \rho S U_{eff}^2 C_l \quad (1)$$

Each of these factors, except density, is controlled by different parameters of the wing morphology and kinematics. The speed of the wing is determined by the combination of flight speed and flapping speed, with the latter being determined by the amplitude and frequency of the wing beat. Wing area can be controlled by retracting or extending the wing. Finally, the lift coefficient depends on the shape of the wing profile (e.g. camber and thickness) and the angle of attack, the angle between the chord line and the direction of the airflow.

To have a more clear understanding of the correlation between the wing kinematics and aerodynamic variables, a detailed explanation has been presented for the effect of these variables on the wing morphology and the performance of the bat.

Wing Speed

Due to the strong dependency of generated aerodynamic lift on speed of the wing, bats are expected to alter their kinematics and wing morphology across flight speeds to generate sufficient weight support and thrust.

The stroke plane angle (β), increases from less than 30° at low to about 75° at high flight speed [15], indicating a change from a horizontal to a more vertical stroke plane (as depicted in fig.1) while the downstroke ratio and span ratio, both increases when going from low to medium flight speed and then decreases slightly when flight speed is increased further,

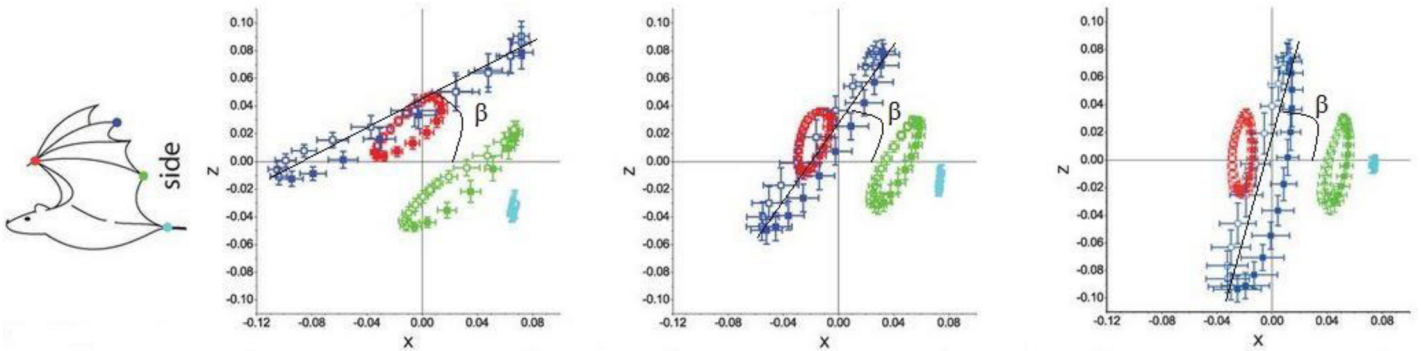


Fig.1. The trace of the wrist (red), the wingtip (blue), the tip of the 5th finger (green) and the foot (sky blue) for one wing beat with the shoulder as the origin for three different speeds (0 m/s, 3 m/s, 7 m/s respectively). Filled symbols represent the downstroke, open symbols the upstroke. The variation of stroke plane angle is clearly visible varying from around 30° at low speeds to 75° at the high speeds. All distances are shown in meter [15].

while the body angle is relatively constant throughout the stroke across speeds, with higher body angle at low speeds.

The wing area varies sinusoidally over the wing beat cycle with the largest area found at the time of mid-downstroke while the lowest is present in the middle of the upstroke. On increasing the flight speed both the minimum and maximum areas tend to decrease slightly and increase on decreasing the flight speed. The innermost part of the wing is aerodynamically relatively inactive at the lowest flight speed range due to the low speed of the flow across the wing, but potentially more important at intermediate flight speeds when the upstroke is more or less inactive [17].

A higher angle of attack produces higher lift, but also higher drag, and therefore the bats are expected to reduce the angle of attack with increasing flight speed when the demand of a high lift coefficient is reduced (as shown in fig.2).

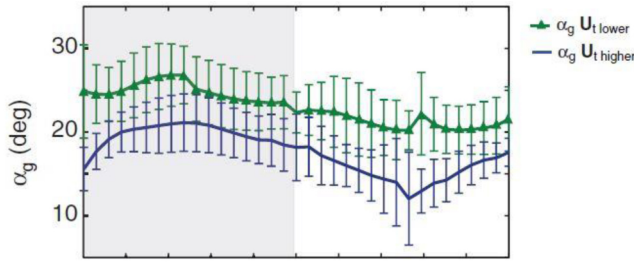


Fig.2. Geometric angle of attack, vertical wrist and wingtip excursion at lower and higher wind speeds averaged over four bats. Grey shading indicates downstroke [12].

The leading edge flap angle has a very large variation with the flight speed, varying from around 5° at high speeds to around 25° at low speeds, with an increase in the lift force during the downstroke, and a decrease during the upstroke. At high speeds, the entire upstroke shows negative values.

The mean angular velocity directly affects the performance of the flyer. It shows a minimum at the speed of

maximum lift to drag ratio, suggesting a simple way to determine the optimal speed from kinematics alone.

The wing velocity (V) is a function of forward velocity (U_∞) and flapping velocity (V_f) as given by equation (2) [18] :

$$V = \sqrt{U_\infty^2 + V_f^2} \quad (2)$$

Forward velocity

Several changes in the kinematics of bats are being observed with changes in the flight velocity. The horizontal velocities of bats are much greater than vertical velocities, so flight paths are more close to horizontal [2]. When flight speed is reduced, sustaining weight support becomes more demanding and bats need to compensate for the lower velocity over the wings by increasing the wing area, flapping speed or lift coefficient. This is particularly important during hovering and slow flight.

Flapping velocity

The flapping velocity of the wing is determined by the stroke amplitude (ϕ_0) and the flapping frequency of the wing beat (f) given by the equation (3) [18]:

$$V_f = 4f\phi_0 R \quad (3)$$

where R is the half of the total wingspan of the wing.

Amplitude

The vertical amplitude of the wing beat increases with increasing the speed while the horizontal amplitude decreases (as shown in fig.3). The angular amplitude in the stroke plane follows a U-shaped pattern with high values at low flight speed, with decreasing and then increasing values with increasing speed. It is highest at low speeds at around 90°, drops to 65° at 3 m/s and rises back to about 80° at high speeds [15]. Stroke plane and wing stroke amplitude at the

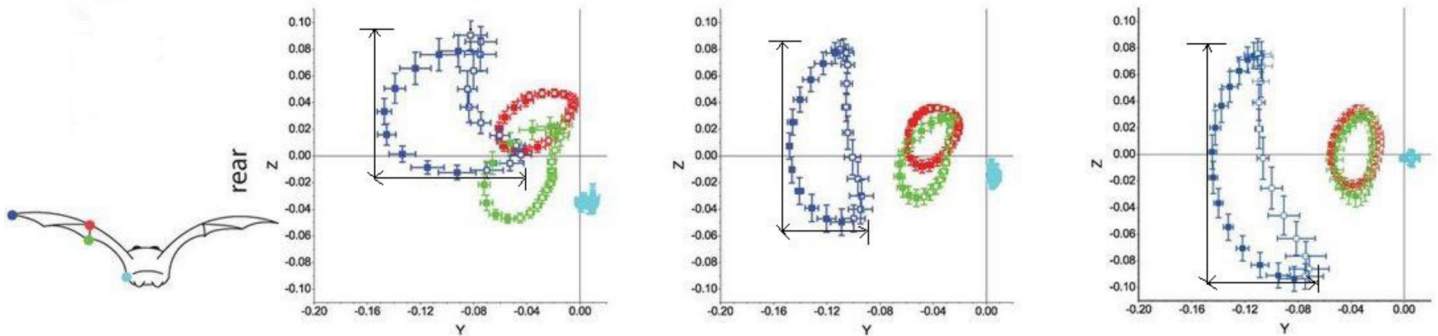


Fig. 3. The trace of the wrist (red), the wingtip (blue), the tip of the 5th finger(green) and the foot(sky blue) for one wing beat with the shoulder as the origin for three different speeds (0 m/s, 3 m/s, 7 m/s respectively). Filled symbols represent the downstroke, open symbols the upstroke. The variation in the stroke amplitude is clearly visible with the vertical amplitude increasing and the horizontal amplitude decreasing on increasing flight speed. All distances are shown in meter [15].

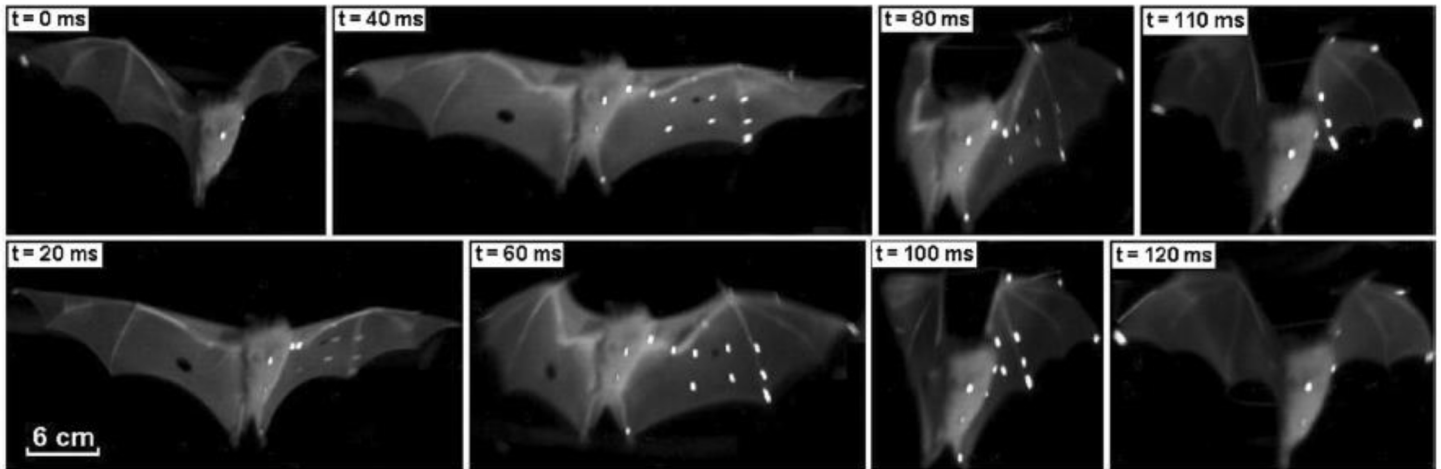


Fig.4. Sequences of images from one high-speed video camera. During the downstroke, the wing is largely extended, although the joints do not reach full extension. During the upstroke, the substantial flexion of elbow, wrist and finger joints is evident [2].

wrist does not change significantly with body mass or wing size.

Flapping frequency

Flapping increases the flight speed of a bat by increasing its Reynolds number as seen from the wings. The wingbeat frequency of bat is about 13.8 Hz during hovering flight and decreases to 10.5 Hz for intermediate and high speeds. It is controlled by the muscular contraction frequency and is expected to decrease with increasing body size [19-20]. The flapping frequency decreases with increasing the flight speed [21, 22, 23]. Small variations in the flapping frequency of consecutive wing beat cycles led to a variable number of computed values of the velocity field and circulation during each cycle [1].

Wing Area

A bat's wing comprises of highly compliant skin membranes that interconnect a jointed skeleton capable of many degrees of freedom. By its very morphological

structure, the area of a bat wing is highly variable throughout every wingbeat cycle. As a result, measurements of the wing area for bats can vary substantially when compared with those of the insects or birds, depending especially on the degree to which the membrane is stretched before measurement.

The area of the wing is largely controlled by the angle between the hand wing and the arm bones. The area of a bat's wing varies sinusoidally throughout the wingbeat cycle and depends greatly on the positions of the carpus and elbow, and the degree of extension and abduction of the digits. The large bats extend the wing more fully on the downstroke, but not on the upstroke, with the largest area found at the time of mid-downstroke while the lowest is present in the middle of the upstroke (see fig. 4). This makes sense, since the majority of lift production occurs on the downstroke. On increasing the flight speed both the minimum and maximum areas tend to decrease slightly, and increase on decreasing the flight speed.

Lift Coefficient

The most general mechanism for increasing the lift coefficient is to increase the angle of attack (AoA). In addition, potential high-lift features, such as high camber of the wing [24-25] and the use of the leading edge vortices, being generated by leading edge flaps, are well known mechanisms to increase the lift coefficient. It improves the gust alleviation and dynamic stall of the wing by increasing the stall angle of attack, which is very important in case of hovering. The variation in camber and AoA is possible due to flexible bones and dozens of joints present in the membrane of the bat wing. Studies suggest that flexible airfoils have greater thrust/input power ratio than rigid airfoils. A thinner airfoil (generally $t/c < 0.06$) with sharp leading edge shows much better results.

The leading edge flap increases both the effective angle of attack and camber of the wing, thus contributing towards increasing the lift force of the wing. The leading edge flap angle varies during the entire wing beat at all speeds, with the flapping pattern being consistent. The angle is mostly positive during the downstroke with more constant values than the upstroke, during which the angle is mostly negative. An increasing deflection of the leading edge with decreasing speed suggests a higher lift coefficient at lower flight speeds. The deflection of the leading edge flap also increases the curvature of the front part of the wing, which would promote the separation of the flow, similar to what has been suggested as the function of the alula in landing steppe eagles [26], and facilitates the generation of the leading edge vortices at low speeds. Moreover, the leading edge vortices [27], produced by flap motion, stay attached to the wing during the downstroke and contribute up to 40% of the total lift at mid-downstroke at low flight speeds.

Angle of attack

When it comes to controlling the lift coefficient of the wing, the angle of attack (α) and camber are considered to be among the most important factors [16]. The angle of attack of the outer wing stays nearly constant during the downstroke, with higher values for lower speeds and decreases during the upstroke until mid-upstroke, with minimal values for low speeds. For all speeds, the angle of attack is positive during the downstroke and negative during the upstroke. The highest values of the angle of attack are reached for hovering flight (80° to -60°). Although steady aircraft airfoils show stall and loss of lift already above an angle of attack of about 15° at these Reynolds numbers [25], the bats operate at mean downstroke angles of attack up to 50° [11,15, 28, 29, 30] without apparent lift loss [30]. This suggests that bats must have some mechanisms to maintain lift throughout the downstroke at these high angles of attack. AoA increases significantly with body mass and the overall change occurs as a result of changes in α_1 but not α_2 (shown in fig. 5) [11].

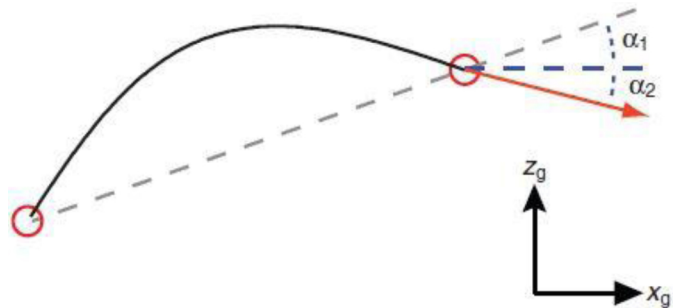


Fig.5. Angle of attack (α) is calculated as $\alpha_1 + \alpha_2$, where α_1 is the angle of the wing chord line above horizontal (blue dashed line), and α_2 is the angle between horizontal and the velocity vector of the wrist (red arrow) in the x_g - z_g plane [11].

Camber

Wing camber is a dynamically changing variable. It is controlled by multiple mechanisms along the span, including the deflection of the leg relative to the body, the bending of the 5th digit, the deflection of the leading edge flap and the upward bending of the wingtip. All of these measures vary throughout the wingbeat suggesting active or aeroelastic control. The camber of the outer wing is mainly controlled by the leading edge flap, the flexion of the phalanges of the 5th digit and the bending of the 5th digit. Since the wing camber is being controlled by a number of mechanisms and parameters, thus it seems to have a large impact on the performance of a bat flight.

The camber has a very large variation during downstroke and upstroke at low flight speeds while it remains constant over time at higher speeds. The slaking of the wing membrane results in a more favorable camber of the outer wing during the supinated upstroke. A passive mechanism for camber control at the outermost part of the wing may be the bending and sweeping of the wing tip. At the outermost part of the wing the fingers run more closely in the spanwise direction than in the chordwise direction, making camber control by the fingers, similar to the 5th digit, less likely. Due to the flexibility of the finger bones [31,32], both the bend and sweep of the wingtip are affected by the aerodynamic forces on the wing and could passively affect the camber of the outer wing [33], while the camber of the innermost part of the wing is actively controlled by the tail-to-body angle.

Body Mass/ Wing Size

Many aspects of wing kinematics vary with body size, but the way kinematics change with velocity and acceleration is relatively consistent with body sizes. The body mass has a direct relationship with the downstroke, which helps to offset the consequences of higher wing loading that accompany increased body size. Larger bats open their wings more completely than smaller bats do in flight [11] and have higher

lift coefficient to compensate for the increase in the body mass. This highlights the importance of wing posture as a confounding variable for hypothesis about ecological function based solely on two-dimensional shape of an outstretched wing. Thus aspect ratio of bats is generally quite low as a large component of lift is generated by tip vortices at low AR. Wing loading as well as the speed at which bat flies increases with the size of the bat, but in the mass range of 0.020 to 0.1 grams, it makes negligible difference.

Angle of attack increases significantly with the increment in body size. The influence of body size on locomotion is no less striking, and biomechanical investigations have revealed that just as body shape changes with size, so do locomotor's kinematics [34, 35, 36].

Concluding Remarks

The aerodynamic lift generated by a wing is proportional to the square of the local speed of the wing, i.e. the vector sum of the forward flight speed and the flapping speed of the wing. Altering flight speed changes the forward velocity component over the wing, and bats alter the kinematics to sustain weight support and to generate sufficient thrust. The unique flexibility and controllability of bat wings suggest a multitude of mechanisms to control the lift generated by the wing. Using this study, it is concluded that all parameters that adjust lift, namely flight speed, wing area and the lift coefficient, are adjusted on account of changing each other. The flapping speed of the wing, which has the largest impact on lift production, shows a U-shaped pattern across flight speed. Wing area is highest during the downstroke and also increases with decreasing flight speed. The lift coefficient is determined by the camber and angle of attack of the wing, which both increase with decreasing flight speed. The angle of attack is highest during the downstroke, hovering and at low flight speeds, increasing the probability of unsteady mechanisms being used to further increase the lift [27]. The studies show an increasing camber with decreasing speed for all positions along the span, until the transition speed when the wing is flipped upside down with a more complex change of camber at lower speeds. The studies also suggest that the bats adjust kinematics to control the flow over the wings and to reduce the drag generated. The bats alter their stroke plane angle, in order to maintain favourable flow characteristics across flight speeds [30].

RESULTS

Maintaining weight support and generating thrust to overcome drag are the main challenges in level flapping flight. After having a detailed study of the effects of every flapping parameter variation, it is concluded that bats vary their wing camber and angle of attack during the entire wingbeat cycle to enhance their performance, which makes their flight most complex. Variation in any one of them results in changing the overall coefficient of lift. This unique

flexibility and controllability of their wings allow bats to alter the flight speed and wing area during flight.

The change of lift coefficient with angle of attack for different wing cambers is being analyzed using unsteady thin airfoil theory, which is an inviscid theory ignoring thickness and applies the linearized boundary condition on a mean surface. Results of the variation of the lift coefficient with angle of attack for 6, 7, 8, 9, and 10% cambers at $Re = 1 \times 10^5$ are being plotted in fig. 6 and compared with the results obtained by Null [37]. It is clearly evident from the results that the lift coefficient C_L is highest for 10% camber airfoil at this Reynold's number, and the slope of the lift curve increases with the wing camber. Computational results show some discrepancies when compared with the experimental data, because of the limitations of the unsteady thin airfoil theory and computational errors. For all cambers, there is negligible difference in C_{Lmin} values of computational and wind tunnel data but a quite significant difference of 0.4 occurs in the C_{Lmax} values. Due to the fact that this is an inviscid theory and doesn't predict the flow separation and stall phenomenon, it results in computing larger values of lift coefficient than the experimental results for high angle of attack, still the theory can be unquestionably used for low values of angle of attack.

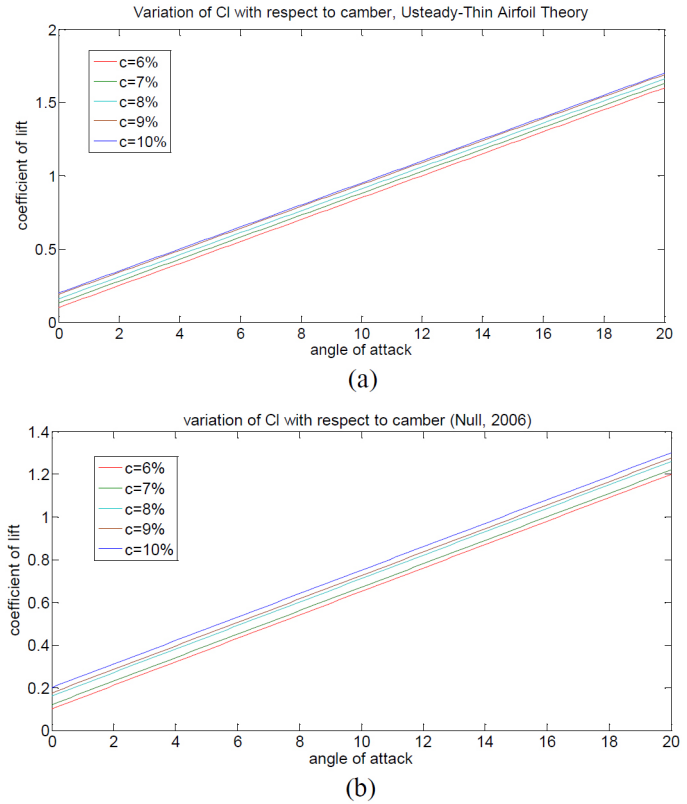


Fig.6. Variation of lift coefficient with 6,7,8,9 and 10% camber thickness by (a) unsteady thin airfoil theory, (b) wind tunnel data, Null [37].

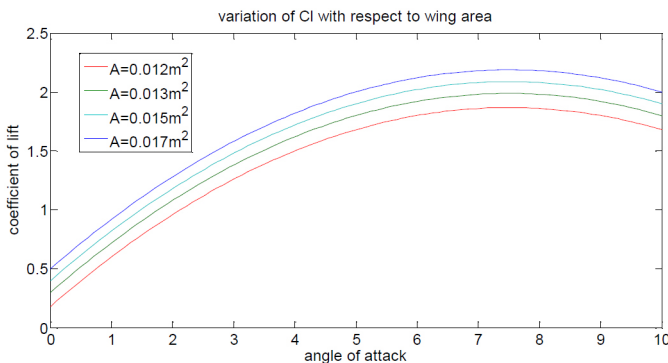


Fig.7. Variation of lift coefficient with different wing areas

In bats, mass is directly proportional to the wing size. Although the wing area increases on account of increasing the wing mass, increasing the lift force, but the increment is not sufficient to compensate for the increased weight, and hence bats increase their lift coefficient by increasing their wing camber and angle of attack. The effect on lift coefficient is being analyzed for different wing areas by using the vortex lattice method [38], and the results are plotted in fig. 7. It is clearly evident from the figure that the lift coefficient increases with the wing area to support the added weight. The results are also in conjugation with the biological data of the species: *Plecotus auritus*, *Leptonycteris yerbabuenae* and *Cynopterus brachyotis*, where wing span increases with the body mass [2, 15, 39, 40, 41].

CONCLUSION

In this study, it is concluded that the bats' flight is the function of various kinematic variables. All parameters that adjust lift, namely flight speed, wing area and the lift coefficient are adjusted on account of changing each other. The lift coefficient mainly depends on the angle of attack and wing camber, which is largely controlled by active deformations in the highly flexible wing membrane. The lift coefficient increases on increasing the wing camber, the effective angle of attack and the wing area.

ACKNOWLEDGEMENTS

The authors would like to acknowledge and thank Prof. Frank Janser (FH Aachen UAS, Germany) for his valuable suggestions and guidance, Eugen Neu (Ph.D. scholar, FH Aachen UAS, Germany), for his assistance and support in computational analysis of the results, Vishnu Ganesh for his significant help in reviewing the paper and finally our wonderful parents.

REFERENCES

1. Hubel Tatjana Y. et al, "Time-resolved wake structure and kinematics of bat flight", *Exp. Fluids*, Springer-Verlag 2009
2. Tian Xiaodong et al, "Direct measurements of the kinematics and dynamics of bat flight", *Bioinspiration & Biomimetics*, 2006

3. Vaughan T. A., "The skeletal system the biology of bats", Vol 1, Ed. Wimsatt W. A. (New York: Academic) pp 98-139, 1970
4. Swartz S. M., "Allometric patterning in the limb skeleton of bats: Implications for the mechanics and energetics of powered flight", *J. Morph.* 234 277-94, 1997
5. Swartz S. M. et al, "Wing bone stresses in free flying bats and the evolution of skeletal design for flight", *nature* 359 726-9, 1992
6. Swartz S. M. et al, "Dynamic complexity of wing form in bats: Implications for flight performance functional and evolutionary ecology of bats", Ed. Akbar Z., McCracken G. and Kunz T. H. (Oxford: Oxford University Press), 2005
7. Riskin D. K. et al, "Quantifying the complexity of bat wing kinematics", *J. Theor. Biol.* 254:604-615, 2008
8. Pennycuick C. J., "Power requirements for horizontal flight in the pigeon: Columba Livia", *J. Exp. Biol.* 49:527-555, 1968
9. Rayner J.M.V., "A vortex theory of animal flight, Part 2: the forward flight of birds", *J. Fluid Mech.* 91:731-763, 1979
10. Tobalske B.W., Hedrick T. L., Dial K. P., Biewener A. A., "Comparative power curves in bird flight", *Nature* 421:363-366, 2003
11. Riskin Daniel K., Iriarte-Díaz José, Middleton Kevin M., Breuer Kenneth S. and Swartz Sharon M., "The effect of body size on the wing movements of pteropodid bats, with insights into thrust and lift production", *The Journal of Experimental Biology* 213, 4110-4122, 2010
12. Hubel Tatjana Y., Riskin Daniel K., Swartz Sharon M. and Breuer Kenneth S., "Wake structure and wing kinematics: the flight of the lesser dog-faced fruit bat, *Cynopterus brachyotis*", *The Journal of Experimental Biology* 213, 3427-3440, 2010
13. MacAyeal Leigh C., Riskin Daniel K., Swartz Sharon M. and Breuer Kenneth S., "Climbing flight performance and load carrying in lesser dog-faced fruit bats (*Cynopterus brachyotis*)", *The Journal of Experimental Biology* 214, 786-793, 2011
14. Riskin Daniel K., Bergou Attila, Breuer Kenneth S. and Swartz Sharon M., "Upstroke wing flexion and the inertial cost of bat flight", Royal society publishing, 2012
15. Rhea et al, "Kinematics and wing shape across flight speed in the bat, *Leptonycteris yerbabuenae*", *Biology Open* 1, 1226-1238, 2012
16. Anderson J. D., "Fundamentals of Aerodynamics", p.772. New York: McGraw-Hill, 1991
17. Johansson L. C., Wolf M., Von Busse R., Winter Y., Spedding G. R. and Hedenstrom A., "The near and far wake of Pallas' long tongued bat: *Glossophaga soricina*", *J. Exp. Biol.* 211, 2909-2918, 2008
18. Lentink Stefan R. et al, "The scalable design of flapping micro-air vehicles inspired by insect flight", *Flying Insects and Robots*, 2009
19. Pennycuick C. J., "Modelling the flying bird", p. 480. Amsterdam: Academic Press, 2008
20. Bullen R. D. and McKenzie N. L., "Scaling bat wingbeat frequency and amplitude", *J. Exp. Biol.* 205, 2615-2626, 2002
21. Schnitzler H. U., "Fledermaus im Windkanal", *Z. Vgl. Physiol.* 73, 209-221, 1971
22. Lindhe Norberg U. M. and Winter Y., "Wing beat kinematics of a nectar feeding bat, *Glossophaga soricina*, flying at different flight speeds and strouhal numbers", *J. Exp. Biol.* 209, 3887-3897, 2006
23. Hubel T. Y., Hristov N. I., Swartz S. M. and Breuer K. S., "Changes in kinematics and aerodynamics over a range of speeds in *Tadarida brasiliensis*, the Brazilian free-tailed bat", *J. R. Soc. Interface* 9, 1120-1130, 2012
24. Norberg U. M., "Bat wing structures important for aerodynamics and rigidity (Mammalia, chiroptera)", *Zoology* 73, 45-61, 1972
25. Laitone E. V., "Wind tunnel tests of wings at reynolds numbers below 70 000", *Exp. Fluids* 23, 405-409, 1997
26. Carruthers A. C., Thomas A. L. R. and Taylor G. K. "Automatic aeroelastic devices in the wings of a steppe eagle *Aquila nipalensis*", *J. Exp. Biol.* 210, 4136-4149, 2007
27. Muijres F. T. et al, "Leading-edge vortex improves lift in slow-flying bats", *Science* 319, 1250-1253, 2008
28. Norberg U. M., "Aerodynamics, kinematics and energetics of horizontal flapping flight in the long-eared bat *Plecotus auritus*", *J. Exp. Biol.* 65, 179-212, 1976
29. Aldridge H. D. J. N., "Kinematics and aerodynamics of the greater horseshoe bat, *Rhinolophus ferrumequinum*, in horizontal flight at various flight speeds", *J. Exp. Biol.* 126, 479-497, 1986
30. Wolf M., Johansson L. C., Von Busse R., Winter Y. and Hedenstrom A., "Kinematics of flight and the relationship to the vortex wake of a Pallas' long tongued bat (*Glossophaga soricina*)", *J. Exp. Biol.* 213, 2142-2153, 2010
31. Swartz S. M., "Allometric patterning in the limb skeleton of bats: Implications for the mechanics and energetic of powered flight", *J. Morphol.* 234, 277-294, 1997
32. Swartz S. M., Bishop K. and Ismael-Aguirre M. F., "Dynamic complexity of wing form in bats: Implications for flight performance", In *Functional and Evolutionary Ecology of Bats*, (ed. Akbar Z., McCracken G. F. and Kunz T. H.), 2006

33. Neuweiler G., "The biology of bats", New York: Oxford University Press, 2000
34. Biewener A. A., "Allometry of quadrupedal locomotion: The scaling of duty factor, bone curvature and limb orientation to body size", *J. Exp. Biol.* 105, 147-171, 1983
35. Biewener A. A., "Biomechanical consequences of scaling", *J. Exp. Biol.* 208, 1665-1676, 2005
36. Heglund N. C. and Taylor C. R., "Speed, stride frequency and energy cost per stride: How do they change with body size and gait?", *J. Exp. Biol.* 138, 301-318, 1988
37. Null W. and Shkarayev S., "Effects of camber on the aerodynamics of adaptive wing micro air vehicles" 2nd AIAA Flow control conference, Portland, Oregon, June 28-1, 2004.
38. Hall K. C., Hall S. R., "A rational engineering analysis of the efficiency of flapping flight", In Fixed and Flapping Wing Aerodynamics for Micro Air Vehicle Application, Progress in Astronautics and Aeronautics, Vol. 195, pp. 249-274. New York, NY: Academic Press, 2002
39. Horner M. A., Fleming T. H. and Sahey C. T., "Foraging behaviour and energetics of a nectar-feeding bat, *Leptonycteris curasoae* (Chiroptera: Phyllostomidae)", *J. Zool.* 244, 575-586, 1998
40. Iriarte-Díaz J. and Swartz S. M., "Kinematics of slow turn maneuvering in the fruit bat, *Cynopterus brachyotis*", *J. Exp. Biol.*, 211 3478-89, 2008
41. Iriarte-Díaz J., "Flight performance in bats and its ecomorphological implications", PhD Thesis, Department of Ecology and Evolutionary Biology, Brown University, 2009



Computational Analysis of 3D Unsteady Flow Over Flapping Wing

2013-01-2098
Published
09/17/2013

Sparsh Sharma and Gaurav Bindal
Vellore Institute of Technology

Copyright © 2013 SAE International
doi:10.4271/2013-01-2098

ABSTRACT

This paper summarizes the complex unsteady, 3-D viscous flow aerodynamics (dominantly laminar) developed in flapping wing generating vortices and intersecting with them. Different flying creatures, (Insects, Birds, and Bats) flapping wing mechanisms are studied and hence being compared based on their wing kinematics and aerodynamic efficiency. The performance of low Reynolds number flyers is highly influenced by the wing shape, wing size, wing camber, aspect ratio, % camber thickness, elastic deformation, wing-beat frequency and wing twisting. The Computation technique used to analyze the wake characteristics of a flapping motion shows that the generation and shedding of vortices dominate the aerodynamic loading on the wing. The periodicity of the wing motion and the resultant vortices leads to conclude that any quantitative model must be based on unsteady aerodynamics and vortex dynamics.

The preliminary assessment of the plan form and the airfoils are performed using Modified Blade Element Theory. Classical blade element theory has been successfully developed for analyzing insect wing aerodynamics, at least for the steady flow contribution. This eliminates small angle assumption and allows accurate calculation of vortex displacement velocity. The focus has been given on the study of sensitivity of the flow to the variation owing kinematics, change in wing plan form shape, airfoil shape and their distribution along the wingspan. Time-accurate Navier-Stokes solvers are employed for the preceding analysis. Even though the flow discovered in natural flyers is mainly laminar, for design perspective it is prudent to include turbulence modeling.

INTRODUCTION

The flapping flight is certainly the most complicated among all flight regimes, fixed, rotary and flapping wings, because of the structural movement and the resulting unsteady fluid dynamics. In biological flight, the wings not only move forward relative to air, they also flap up and down, plunge, and sweep in order to deal with any disturbances like gusts, etc. that can dramatically change the aerodynamics around the wings[1, 2, 3, 4, 5]. To produce aerodynamic effects in ways that an aileron on the wing of a conventional plane does, birds have the supination and pronation mechanism in which one wing is twisted downward to reduce angle of attack (AoA) and corresponding lift while the other one is twisted upward to increase the lift. A bird is able to roll by performing different degrees of twisting between wings [1].

Birds with large wingspan, like eagle and osprey, usually glide and soar at high Reynolds number and have a large lift-to-drag ratio of 19, hence the aerodynamic model of their wings can be assumed as Quasi-steady aerodynamic model. Moreover, their flapping frequency is also quite low, making viscous effects less significant, almost negligible, which results in less time consuming calculations with little compromises in results. Whereas in small wingspan envelope, like that of hummingbird, bat, dragonflies etc, the flow is perfectly unsteady and viscous effects can't be neglected. This leaves no room for quasi-steady model and instead computation involving turbulence modeling is preferred.

Numerous analyses in past were based on inviscid flow; Greenewelt [6] assumed an elliptical lift distribution with suitable correction factors to model bird flight and proceeded to estimate power and drag coefficients for various bird species [6][7]. Pennycook [8][9] theorized that a steady

actuator disk producing constant momentum flux could represent the flapping wing and its aerodynamic force generation. Waldman [10] did a computational analysis of bat like membrane in XFOIL. An unsteady 3-dimensional incompressible Navier-Stokes equation was chosen as the computational model for the analysis of flapping wing by Yang-yao Niu [11]. Simulations of vortex behaviors and forces due to the reduced frequency of the 3D flapping wings are investigated and numerical results of flapping NACA0012 wing are verified with experimental data. In a recent work by Garcia [12], a lifting-line analysis based on Weissinger's method for straight swept wing was used to solve the problem. Smith [13] simulated the 3D unsteady flow field around a tethered moth wing and emphasized the importance of including the effect of the wake in the analysis. A 2D model by Wang [14] investigated the vortex shedding and found an optimal flapping frequency based on the time scale associated with shedding of the leading edge and trailing edge vortices.

All the major computational analyses done are listed above. Furthermore, all of them used either a quasi-steady model or neglected the viscous effects, sufficient enough to imply that their results are somehow approximated as one and a space for refinement exists. It was Ellington [15], however, showed that these quasi-steady analyses do not correctly predict the forces magnitudes, particularly the lift coefficient. A major limitation of steady or quasi steady analysis is that the motion of the wings causes an inherently unsteady wake with large vortices generated on the wing. Now if the reduced frequency is lesser than unity, which means flapping frequency is lesser the forward flight then the unsteadiness of the kinematics might be muted for the quasi-steady assumption to remain valid. However, if this reduced frequency exceeds unity then the flight would certainly invalidate the quasi-steady assumption as the flow field is then inherently unsteady in nature.

An exact solution to the problem is still not present due to the considerable complexity of the flapping flight. To adapt or mimic the amazing flight performance of natural flyers, one needs to have a complete understanding of the flow physics involved. A complete model of the system requires not only a prediction of the unsteady aerodynamics, but also a description of the time and geometry dependent aero elastic interactions between the wing and the flow field [7].

This paper is the first in series of our research on BAT inspired Micro Air Vehicle (MAV). The investigation is particularly focused on unveiling the sensitivity of flow to variation of

- airfoil shape
- wing planform shape
- wing aerodynamics and kinematics

All the tests and analyses are done assuming unsteady flow regime without neglecting the viscous effects.

FACTORS AFFECTING LOW REYNOLDS NUMBER AERODYNAMICS

When studying natural flyers, it is insightful to assess the effects of different parameters, such as wing area and wing span, on the flight characteristics, based on dimensional analysis [3][16, 17, 18, 19]. The preferred airfoil shapes for low Reynolds number regime are quite different from those typically used for high Reynolds number manned aircraft. The range of the AoA within which the aerodynamic performance of the flyer is satisfactory, becomes narrower as the Reynolds number decreases. The aerodynamic performance in a low Reynolds number wing is highly affected by the induced drag generated by the tip vortex, which not only affects its lift and drag but also the potential flight stability. Within the low Reynolds number range, different flyers exhibit different approaches for better aerodynamic performance. A thinner airfoil is more preferable in the range of 10^6 to 10^4 as the maximum lift-to-drag ratio decreases abruptly in this range and a thinner airfoil with modest camber generates a better lift to drag ratio with better power efficiency. With Reynolds number in the range of 10^4 and 10^3 , a corrugated wing can provide a more favorable lift than a non corrugated wing because the viscous effect substantially modifies the effective airfoil shape and reduces the effective AoA [16]. In addition to the Reynolds number, the aerodynamic performance of a natural flyer is highly influenced by numerous parameters such as the wing shape, wing size, wing camber, percent camber thickness and wingbeat frequency.

Wing Camber

Low camber has the advantage of delaying flow separation on the underside of the wing at high speeds and very low angle of attack. As the camber increases, the lift coefficient slope and the maximum lift coefficient increases as well [16]. The increase in camber pushes both the maximum lift coefficient and maximum lift-to-drag ratio to a higher AoA [16][20] along with increasing the stall angle of the wing. Low cambered airfoil has high stall-resisting capability and is less sensitive to the AoA which eliminates the need of any sophisticated steering. The drag coefficient of low cambered is also high when compared with high cambered airfoil but lift force levels after a particular angle allowing it to attain high AoA without stalling. Sunada [21] compared the wing characteristics at a Reynolds number of 4×10^3 and concluded that the wing performance can be improved with a modest camber of around 5% [16]. Both lift and drag coefficients increase as the position of the maximum camber approaches the trailing edge of the wing [16][20][21] but the maximum value of lift-to-drag ratio is obtained at 25% chord position of maximum camber. Also after having a detailed study of the wing thickness, it is concluded that increasing the thickness of the wing deteriorates the wing aerodynamic characteristics.

Wing Shape

Unlike conventional airfoils, which are smooth and streamlined, natural flyers are born with different airfoil shapes with diversified geometries which improve their aerodynamic performance. Insects have rough surface airfoils which bear both structural and aerodynamic benefits to them [16][22][23]. The corrugations of the dragonfly wings and the scales on the wing surface of butterfly and moth are of critical importance to the stability of its ultra light construction and in visualizing experiments using corrugated wings. The reason, as suggested by Kesel [24], is that vortices fill the profile valleys formed by these bends and therefore smoothen the profile geometry [16][25]. In the comparison done for the aerodynamic characteristics of dragonfly wing sections with conventionally designed airfoils and flat plates, it is concluded that corrugated airfoils have very low drag coefficients closely resembling those of flat plates, whereas the lift coefficients are much higher than those of flat plates [16]. Thus the performance of such a corrugated airfoil is influenced by its “effective” shape, characterized by the viscous effects.

Wing Size

When flapping animals are studied, often the parameters of interest are related to the body mass m of the animal [26][27]. The wing span is given by the following eq. [28]:

$$b = 1.704 * m^{1/3} \quad (\text{birds}) \quad (1)$$

With a larger wing span, flapping velocity increases and changes its direction, which affects the magnitude and direction of relative flow velocity. Because relative flow velocity determines the resulting aerodynamic force acting on each wing section along the span, force will also change in magnitude and direction.

Aspect Ratio

Usually, the agility and maneuverability improves with a smaller AR. This is one of the reasons why military fighter aircrafts and aerobatic airplanes have relatively shorter wingspans compared with those of conventional aircraft. The similar relation is found in natural flyers. The largest AR for birds is found among species that typically spend a substantial portion of their time in soaring flight instead of flapping. Higher AR also tends to decrease the induced drag, which is caused by the lift. Similarly the lift-to-drag ratio L/D, also known as glide ratio, increases with an increasing AR.

Wing Beat Frequency

The upper and lower limits of wing-beat frequency for flapping animals are settled by the power available from flight muscles and the force provided by the wing bones. The main function of wing bones is to transmit force to the external environment during flight [29][30]. This force cannot be too high for the risk of muscle failure. Larger

animals oscillate their limbs at lower frequencies than smaller ones of similar type [31] and the mechanical power produced by a particular flight muscle is directly proportional to the contraction frequency. Thus while explaining the theories of flapping flight; this is one of the important parameters to be looked upon. There is always a natural frequency imposed on the animal by physical characteristics of its limbs and the forces that it must overcome [32]. Based on the insight into the flapping frequency, it is possible to estimate the power output from a bird's flight muscles and achieve an estimation of the power required for flying.

Thus the scaling laws indicate that, as a flyer's size reduces, it has to flap faster to stay up in the air, experiences lower wing loading, is capable of cruising slower, has a lower stall speed, and consequently can survive much better in a crash landing. In the meantime, as a flyer becomes smaller, its weight shrinks at a much faster rate, meaning that it can carry very little “fuel” and has to resupply frequently.

Birds, bats, and insects apply different flapping patterns in hovering and forward flight to generate lift and thrust. Typically, in slow forward flight the reduced frequency and wing-beat amplitude tend to be high, resulting in highly unsteady flow structures. In fast forward flight the reduced frequency and the wing-beat amplitude tend to be low, and the wake often consists of a pair of continuous undulating vortex tubes or line vortices. Larger birds have relatively simple wingtip paths compared with those of smaller flyers. As a flyer's size reduces, its operating Reynolds number becomes lower; accordingly, its wing in a steady stream produces a poorer lift-to-drag ratio. Coupling with a slower flight speed, a small flyer is substantially more influenced by the flight environment such as wind gust. To overcome these challenges, natural flyers flap their wings faster to enhance lift and improve maneuverability [16].

AERODYNAMICS AND WING KINEMATICS OF NATURAL FLYERS

Birds, bats and insects apply a variety of flapping patterns in hovering and forward flight to generate lift and thrust. In this section, the wing kinematics and aerodynamic efficiency of different flying creatures i.e. birds, bats and insects are being presented.

Insects

The range, in which the insects can vary their stroke plane angle, is very large. The wing tip makes different motions depending on the insect, i.e. oval, figure-eight or pear-shaped trajectories [33][34], or combinations of these patterns. Some insects may also change their stroke trajectory for strong manoeuvres. The most simple wing motion is performed by drosophila fruit fly during its hovering [35].

In the most common form of hovering in insects, the wings move along an approximately horizontal stroke plane with approximately equal and relatively high angles of attack

during the downstroke and upstroke [33]. This is being achieved by the fast rotation of the wings at the end of each half stroke. The general pattern has been shown in figure 1. The whole stroke cycle can be described by a sinusoidal motion or a triangular motion depending on the insect. For the Drosophila Melanogaster the stroke trajectory is more of a triangular motion with amplitude of 130-160 degrees and a flapping frequency of 250 Hz [33].

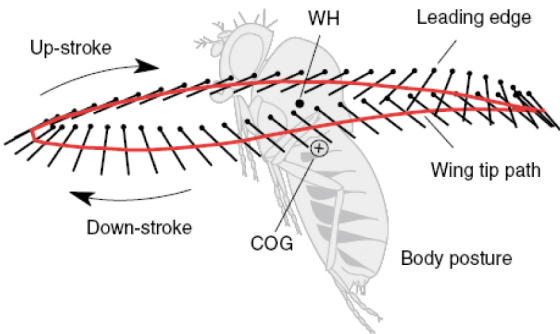


Figure 1. General pattern for the wing motion of *Drosophila Melanogaster* [34]

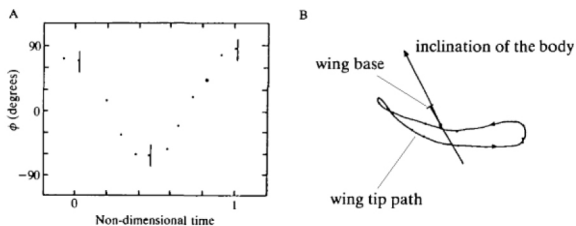


Figure 2. Kinematics of *Drosophila Melanogaster* [35]

(A) Wing tip trajectory in degrees, (B) Wing tip path drawn with respect to the body, which is represented by an arrow

Insects are hovering specialists. They are able to hover by using a range of possible unsteady high-lift mechanisms, including rotational circulation, clap-and-fling and wake capture. However, arguably the most important mechanism is the leading-edge vortex, which may generate up to 66% of the total lift in insect flight [36]. Consequently to create the LEV, the high angle of attack is very crucial for generating enough lift force. The generated lift force highly depends on the stroke trajectory [34]. One can assume that if a wing is moved with the same angle of attack and rotational velocity, the same lift force should occur but different stroke trajectories change the airflow pattern, the created vortices and hence the generated lift force [33].

Birds

Birds usually flap their wings to generate both lift and thrust. But if they stop flapping and keep their wings stretched out, their wings actively produce only lift, not thrust [16]. Thrust can be produced by gravitational force while the animal is descending or gliding. Gliding birds (as well as soaring birds) like vultures, albatrosses, pelicans and storks appear to hang in the air effortlessly, gaining height with barely a twitch of a wing and thus have high lift-to-drag ratio. The gliding angle,

angle between the motion direction and the incoming air, directly controls the lift-to-drag ratio. The higher this ratio, the shallower the glide becomes. Larger birds fly at high Reynolds numbers and have a large lift-to-drag ratio. For example, a wandering albatross, with a wing span of over 3 meters, has a reported lift-to-drag ratio of 19, whereas the fruit fly, which has a span of 6 millimeters, has a lift-to-drag ratio of 1.8 [16][37].

Larger birds have relatively simple wingtip paths. For example, an oval tip path is often associated with albatrosses. Smaller flyers exhibit more complicated flapping patterns.

Flapping involves two stages: the downstroke or power stroke, which provides the majority of the thrust, and the upstroke or recovery stroke, which can also (depending on the bird's wings) provide some upward force [38]. In the upstroke, the wing is slightly folded inwards to reduce upward resistance. Birds change the angle of attack between the upstroke and the downstroke of their wings. During the downstroke the angle of attack is increased, and is decreased during the upstroke. Since the outer part of the wing moves up and down more steeply than the inner part, the wing has to twist (bird's wings are very flexible) so that each part of the wing can maintain just the right angle of attack. As the wing twists and the outer wing part moves downward, the lift force in the outer part of the wing is angled forward. This is what would happen if the whole bird went into a steep dive. However, only the wing is moving downward, not the whole bird. Therefore the bird can generate a large amount of forward propulsive force without any loss of altitude [38]. During this stroke, the air is not only deflected downward, but also to the rear. The air is forced backward just as it would be by a propeller.

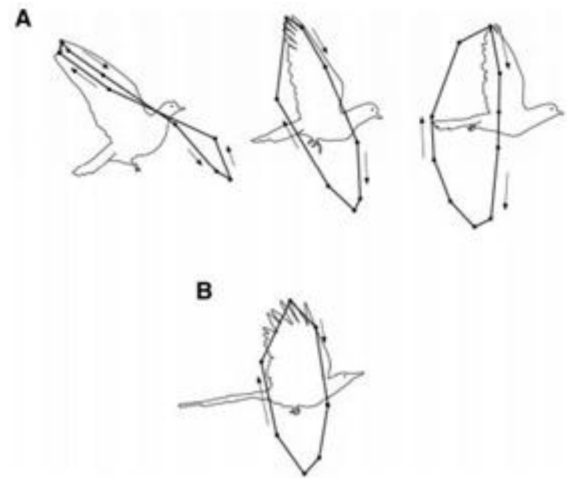


Figure 3. Wingtip paths relative to the body for two natural flyers. (A) Pigeon (*Columba Livia*), the path transition from tip-reversal upstrokes during slow flight to feathered upstrokes at intermediate speeds and a swept-wing upstroke during fast flight. (B) Black-billed magpie (*Pica Hudsonica*) wingtip path at all flight speeds [38].

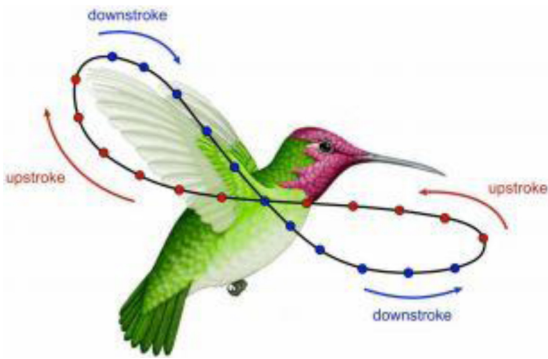


Figure 4. Hummingbird in hovering flight, wing's figure-eight pattern [16]/[38]/[39]

In a hummingbird, it can be seen that the flapping motion is sinusoidal, where the downstroke is performed insignificantly faster than the upstroke.

Hanging, which is generating only lift through flapping rather than a product of lift and thrust, demands a lot of energy. Whether a flying animal can hover or not depends on its size, moment of inertia of the wing, degrees of freedom in the movement of the wing and the wing shape [16][38]. As a result of these limitations, hovering is mainly performed by small birds and insects. Although the kinematics of the wing motion of birds is almost symmetric with that of the insects, it is assumed that the unevenness occurs due to a slight difference in the angular velocity during downstroke and upstroke. A missing leading edge vortex during upstroke and several musculoskeletal and plan form material properties do not allow the bird's wing to behave equally efficient as the insect's wing. For instance, during the downstroke the wing is slightly cambered, while during the upstroke the wing is not capable to invert the camber, which gives a significant loss of the produced lift force in birds.

Bats

Among all natural flyers (birds, bats & insects), bats are proven to be the most superior and efficient flyers due to their complex aerodynamics. Birds and insects can fold and rotate their wings during flight, but bats have many other options. They can generate different wing shapes and motions that other creatures can't. Bat's wings are highly articulated, with more than two dozen independent joints and bones which deform adaptively during the motion of the wingbeat cycle with a thin flexible membrane covering them. This flexible skin can catch the air and generate lift and reduce the drag in many different ways. Besides the anatomical structure of the bat's wing, the changes in the length of the different bones and the membrane also lead to the complex trajectories of the wing motion.

The wing motion is observed to be similar for most of the species of bats [40]. Mainly the study about the Leptonycteris Yerbabunae is considered which gives a sufficient insight into the aerodynamics and kinematic aspects of the bat flight. The general motion is characterized by the cambered wing

during the downstroke, and folding of the wing during the upstroke. During downstroke the wing is approximately stretched, with an almost synchronous movement of all joints.

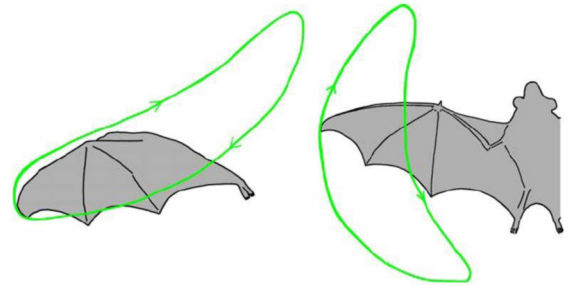


Figure 5. Typical wing tip paths of a bat seen from the side (left) and the top (right)[41]

The lift mechanisms in bat flight, originated from unsteady effects, are not studied in detail yet. The main contribution to the lift force is found to be given by the Leading Edge Vortex [42]. The flow separates at the leading edge, generating an area of high negative vorticity. The airflow reattaches behind this area, resulting in an attached and laminar flow at the trailing edge. The vorticity is stronger near the wingtip and decreases toward the wing root. An area with negative vorticity is developed at the trailing edge of the wing, resulting into a strong rotational movement before the end of the downstroke, and also enhancing lift generation. During the upstroke, the vortex which generates much of the lift in bat flight is not documented well. It does not appear to originate from the wingtips as it does in case of downstroke. According to biologists, the starting point of the vortex seems to be somewhere in the middle of the wing, which again shows that the complex wing structure with numerous joints is crucial for the efficient bat flight.

METHODOLOGY

Modified Blade Element Theory

The quasi-steady limit mainly corresponds to larger birds such as eagle and osprey, which soar and glide. While soaring, the wings are fixed and rigid and act like those of conventional aircraft. For these fliers, flapping is restricted to limited operations, such as take-off, landing, and stabilization. Smaller birds and insects that flap continuously, occupy the other end of the aerodynamic spectrum, that of fully unsteady flight.

The usual aerodynamic treatment of insect flight is based on the blade element theory of propellers, modified by Osborne [43] for flapping flight. The fundamental unit of analysis is the wing element, the portion of the wing between r and $r + dr$ from the wing base. The aerodynamic force F' per unit span on a wing element is resolved into a lift component L' and drag component D'_{pro} . The force components for a wing section per unit span are [44]:

$$L' = \frac{1}{2} \rho c U^2 C_L \quad (2)$$

$$D'_{\text{pro}} = \frac{1}{2} \rho c U^2 C_{D,\text{pro}} \quad (3)$$

where ρ is the mass density of air, c is the chord length and U is the local relative velocity component perpendicular to the longitudinal wing axis.

The induced drag coefficient is not calculated explicitly. Instead, the induced power needed to create the downwash corresponding to the vertical force is estimated independently from the ideal momentum jet of propellers, corrected for spatial variation in loading using the differential momentum jet theory, and for tip effects using a vortex theory. A new method of calculating induced power, based on the added mass of vortex sheets in the wake, gives good agreement with the more traditional approach. Both methods provide an estimate of the downwash velocity in the vicinity of the wings, and this is used to calculate the downwash angle of the relative velocity.

The lift and drag forces are resolved into vertical and horizontal components, integrated all over the wing span, and averaged over the cycle. The net force balance in hovering flight requires the mean vertical force to be equal to the weight and mean horizontal force to be equal to zero.

The mean coefficient method is normally used. By treating the force coefficients as constants over a half-stroke, they can be removed from the double integrals resulting from the manipulation of the equation, and mean values can be found that satisfy the net force balance. The kinematic detail required for this method is greatly reduced since only the motion of the longitudinal wing axis is needed. The mean lift coefficient is particularly interesting because it is also the minimum value compatible with flight. A typical application of the mean coefficient method also ignores the downwash angle. This angle is typically less than 10 deg for hovering flight.

Most modern applications of the mean coefficient method have concluded that the mean C_L required for the weight support exceeds the maximum value for steady flow, sometimes by a factor of 2 or 3. The results show that insect's wing produce more lift than expected from conventional two-dimensional considerations and those high-lift mechanisms are employed instead.

Spring-Based Smoothing

In the spring-based smoothing method, the edges between any two mesh nodes are idealized as a network of interconnected springs. The initial spacings of the edges before any boundary motion constitute the equilibrium state of the mesh. A displacement at a given boundary node will generate a force proportional to the displacement along all the springs connected to the node. Using Hooke's Law, the force on a mesh node can be written as [45]:

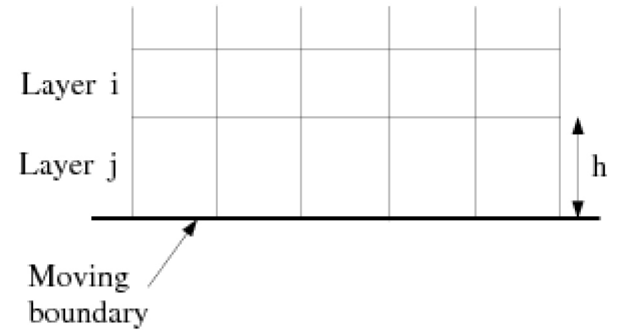
$$\vec{F}_i = \sum_j^{n_i} k_{ij} (\Delta \bar{x}_j - \Delta \bar{x}_i) \quad (4)$$

where $\Delta \bar{x}_i$ and $\Delta \bar{x}_j$ are the displacements of node i and its neighbor j , n_i is the number of neighboring nodes connected to node i , and k_{ij} is the spring constant (or stiffness) between node i and its neighbor j . The spring constant for the edge connecting nodes i and j is defined as

$$k_{ij} = \frac{1}{\sqrt{|\bar{x}_i - \bar{x}_j|}} \quad (5)$$

Dynamic Layering Method

In prismatic mesh zones, dynamic layering method adds or removes layers of cells adjacent to a moving boundary, based on the height of the layer adjacent to the moving surface. The dynamic mesh model in ANSYS FLUENT allows you to specify an ideal layer height on each moving boundary.



If the cells in layer j are expanding, the cell heights are allowed to increase until

$$h_{\min} > (1 + a_s)h_{\text{ideal}} \quad (6)$$

Here h_{\min} is the minimum cell height of cell layer j , h_{ideal} is the ideal cell height, and a_s is the layer split factor.

If the cells in layer j are being compressed, they can be compressed until

$$h_{\min} < a_c h_{\text{ideal}} \quad (7)$$

where a_c is the layer collapse factor. When this condition is met, the compressed layer of cells is merged into the layer of cells above the compressed layer; i.e., the cells in layer j are merged with those in layer i .

Implicit Update Settings

For such applications, having the mesh motion updated within the time step based on the converging flow solution results in a stronger coupling between the flow solution and the mesh motion, and leads to a more robust solver run. Implicit mesh updating allows you to run simulations that otherwise could not be solved or would require an unreasonably small time step.

The relaxation of the displacements is defined by the following equation [45]:

$$x_k = \omega(x_{computed,k}) + (1 - \omega)x_{k-1} \quad (8)$$

where x_k is the node position at iteration k (within a time step), $x_{computed,k}$ is the computed node position (based on the flow field), and ω is the motion relaxation.

LES Initialization

For simulations initialized with values (rather than from an initial guess field), it is possible to perturb the initial guess by setting an RMS Velocity Fluctuation. This has the effect of kick starting the solution process. For a velocity distribution V_i , the fluctuation is the quantity [45]:

$$V_{rms} = \sqrt{\sum_{i=1}^N \frac{(V_i - \bar{V})^2}{N}} \quad (9)$$

This simple model was first proposed by Smagorinsky. In the Smagorinsky-Lilly model, the eddy-viscosity is modeled by [45]:

$$\mu_t = \rho L_s^2 |\bar{S}| \quad (10)$$

Where L_s is the mixing length for sub grid scales and

$$|\bar{S}| = \sqrt{2S_{ij}S_{ij}} \quad (11)$$

L_s is computed using

$$L_s = \min(kd, C_s \Delta) \quad (12)$$

where k is the von Kármán constant, d is the distance to the closest wall, C_s is the Smagorinsky constant, and Δ is the local grid scale. In the calculation, Δ is computed according to the volume of the computational cell using

$$\Delta = V^{1/3} \quad (13)$$

Lilly derived a value of 0.17 C_s for homogeneous isotropic turbulence in the inertial subrange. However, this value was found to cause excessive damping of large-scale fluctuations in the presence of mean shear and in transitional flows as near solid boundary, and has to be reduced in such regions. In short, C_s is not a universal constant, which is the most serious shortcoming of this simple model. Nonetheless, a C_s value of around 0.1 has been found to yield the best results for a wide range of flows, and is the default value in ANSYS FLUENT

Inlet Boundary Conditions for the LES Model

This section describes the algorithm to model the fluctuating velocity at velocity inlet boundaries or pressure inlet boundaries. To generate a time-dependent inlet condition, a random 2D vortex method is considered. With this approach, a perturbation is added on a specified mean velocity profile via a fluctuating vorticity field (i.e. two-dimensional in the plane normal to the streamwise direction). The vortex method is based on the Lagrangian form of the 2D evolution equation of the vorticity and the Biot-Savart law. A particle discretization is used to solve this equation. These particles or “vortex points” are convected randomly and carry information about the vorticity field. If N is the number of vortex points and A is the area of the inlet section, the amount of vorticity carried by a given particle i is represented by the circulation Γ_i and an assumed spatial distribution η [45]:

$$\Gamma_i(x, y) = 4 \sqrt{\frac{\pi A k(x, y)}{3N[2 \ln 3 - 3 \ln 2]}} \quad (14)$$

$$\eta(\vec{x}) = \frac{1}{2\pi\sigma^2} (2e^{-|x|^2/2\sigma^2} - 1) 2e^{-|x|^2/2\sigma^2} \quad (15)$$

where k is the turbulence kinetic energy. The parameter σ provides control over the size of a vortex particle.

RESULTS

The calculations illustrate the current potential of the method and provide an initial insight into the aerodynamic behavior of the flapping wing at a low speed (10m/s) forward flight. The selection of the wing planform, shape of the airfoil forming the wing and the prescribed kinematics of flapping are still open questions at this very stage of the project. The overall aerodynamic aspects of design and thorough understanding of the flow physics will be a subject of long terms. The presented calculations are performed on the planform inspired by the geometrical length and mean aerodynamic chord length of a bat wing [46]. The corresponding planform is shown below:

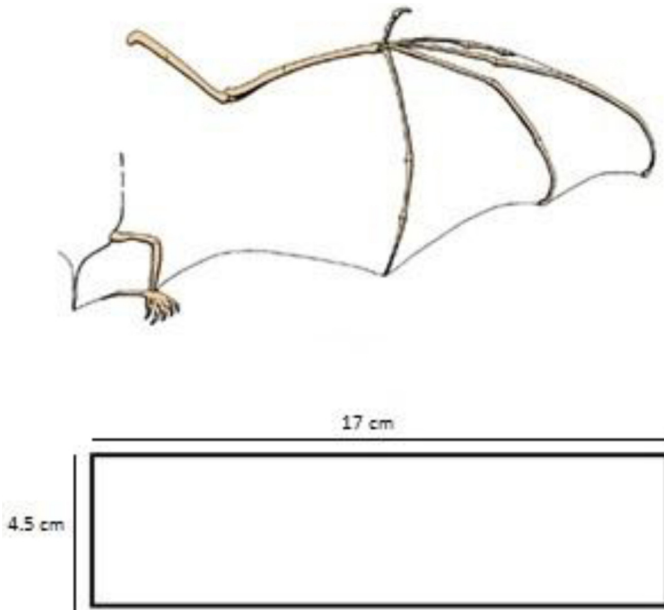


Figure 6. Bat wing and NACA 0010 wing with same mean chord length

It is anticipated from the observation of bats that the design of final airfoil section will result in still much thinner airfoils characterized by sharp leading edge. For present analysis, NACA0010 has been chosen as an appropriate option.

The species chosen for the MAV is Leptonycteris yerbabuenae because there are enough studies available on kinematics of bats. Thus a variety of data from different bats is available. But there are bats, which can fly slow, even hover and some cannot, so it's really important to consider the ecology of the bats when picking the species. If a bat can't fly slowly, it would not be expected to be stable at low speeds and hovering in contrast with a same scale MAV.

Setting of Boundary Conditions

The predetermined MAV flying speed is 10 m/s [47], therefore, incoming air speed is 10 m/s. The outflow is an atmospheric pressure. Since the flow field is assumed to be sliding, the hypothesis of flow passage flank is the sliding boundary. Then, the position boundary will not have the boundary layer effect. The flapping amplitude is 22.5° due to cell limitation. The number of the cells was confined to 512000 due to the academic license agreement. The following figure shows the grid distribution around the wing:

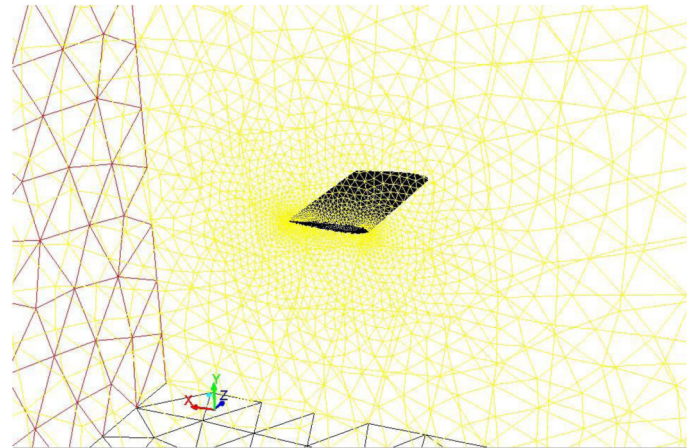


Figure 7. Computational grid distribution near the wing. Fine grid near the wing surface for boundary layer effects

The flapping amplitude angles were interpreted from the kinematics presented in Figure 8 [48].

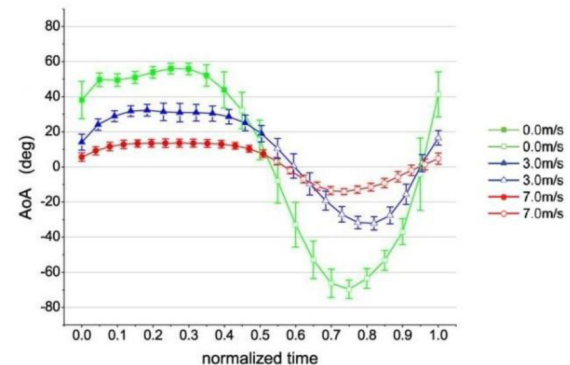


Figure 8. Filled symbols represent the downstroke; open symbols represent the upstroke,

The Navier stokes computations on formerly mentioned turbulence method were performed for an extended range of θ (θ is the flapping angle around x-axis). The variation of pressure coefficient, C_p with wing reference length, X is plotted in Figure 9.

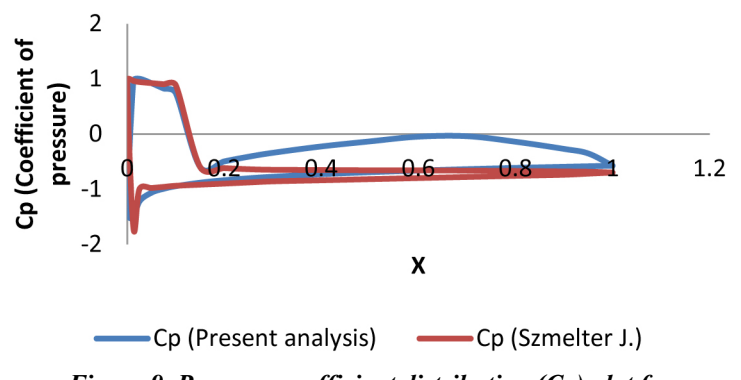


Figure 9. Pressure coefficient distribution (C_p) plot for $\theta=(+)\text{22.5}^\circ$

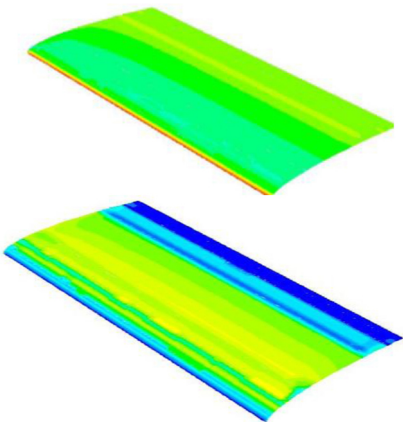


Figure 10. Pressure coefficient and dynamic pressure contour (from top to bottom) for $\theta=(+)$ 22.5°

From Figure 9 and 10, it can be simply observed that at the leading edge, a stagnation is occurring which leads to the formation of Leading Edge Vortex (LEV). On moving towards trailing edge, the C_p value remains almost constant with little fluctuations at around 20% of the chord length. On other hand, in the case of dynamic pressure contour, stagnation is followed by a uniformity of flow or attachment of flow which again goes turbulent at around 60% of the chord length and transforms into vortical flows.

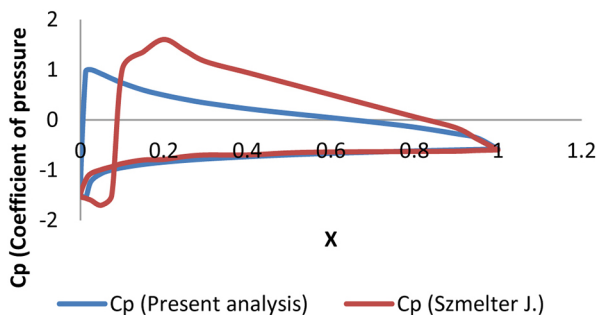


Figure 11. Pressure coefficient distribution (C_p) plot for $\theta = (-)$ 22.5°

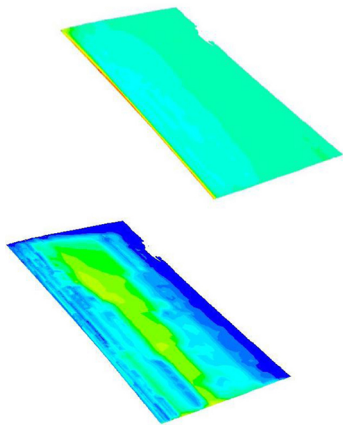


Figure 12. Pressure coefficient and dynamic pressure contour (from top to bottom) for $\theta=(-)$ 22.5°

The plot between coefficient of pressure, C_p and wing reference length, X is shown in Figure 11. As Moving towards the trailing edge reveals a gradual increase in C_p value, this is because the wing is moving from downstroke to upstroke. At 50% of the chord length, a sudden increment can be easily seen in the figure after which it again moves uniformly. However the dynamic pressure contour has more number of fluctuations than the earlier one. In this orientation, the leading edge seems quite stable than the trailing edge and also from the leading edge of the preceding case. A sudden increase of dynamic pressure occurred in the mid of the wing during this phase which is followed by stagnation from all around. Vertical flows can be seen at trailing edge and tip chord.

Both the plots have been compared and validated with the work done by Szmelter J. and Zbikowski R. (Cranfield University, UK) [49].

CONCLUSION

This paper, as mentioned previously, first in series of our research on Bat inspired Micro Air vehicle (MAV), reports the current status of a long term project investigating aerodynamic aspects of flapping MAVs. The presented literature shows, even though the flow discovered in natural flyers is laminar, it is prudent to include turbulence modeling for design perspective. A thorough investigation of the factors affecting the low Reynolds number flight is done. The methodology adopted (Large Eddy Simulations with Spring based smoothing) has been elaborated in detail.

The model provides initial insight into the flow physics and proves that any quantitative model must be based on unsteady aerodynamics and vortex dynamics.

REFERENCES

1. Dial, K. P., "An inside look at how birds fly: Experimental studies of the internal and external processes controlling flight", Report to the Aerospace Profession, 1994
2. Goslow, G. E.Jr., Dial, K. P., et al. "Bird flight: Insights and complications", Bio Science 40, 108-15, 1990
3. Norberg, U. M., "Vertebrate flight: Mechanics, Physiology, Morphology, Ecology and Evolution", 1990
4. Shipman, P., "Taking wing: Archaeopteryx and the evolution of bird flight", 1998
5. Tobalske, B. W. and Dial, K. P., "Flight kinematics of black-billed magpies and pigeons over a wide range of speeds", Journal of Experimental Biology 199, 263-80, 1996
6. Greenewalt, C. H., "The flight of birds: The significant dimensions, their departure from the requirements for dimensional similarity, and the effect on flight aerodynamics of that departure", Transactions of the American Philosophical Society 65 (4), 1-67, 1975
7. Hoa Steven, Nassefa Hany, Pornsinsirirakb Nick, Tai Yu-Chong, et al., "Unsteady aerodynamics and flow control for

- flapping wing flyers”, *Progress in Aerospace Sciences* 39 (2003) 635-681, 2003
8. Pennycuick, C. J., “Mechanical constraints on the evolution of flight”, in Padian K. (Ed.), *The origin of birds and the evolution of flight*, Memoirs of the California Academy of Sciences, Vol. 8, pp. 83-98, 1986
 9. Pennycuick, C. J., “Bird flight performance: A practical calculation manual” (Oxford, UK/New York, Oxford University Press), 1989
 10. Waldman Rye, Riskin Daniel, Swartz Sharon, Breuer Kenneth, et al., “Aerodynamic behavior of compliant membranes as related to bat flight”, *AIAA 2008-3716*, *Biological and Bioinspired Flows-I Biological Locomotion*, 2008
 11. Niu Yang-Yao, Liu Shin-Han, Chang Che-Cheng and Tseng T.I., “A preliminary study of the three-dimensional aerodynamics of flapping wings”, *Journal of Applied Science and Engineering*, appeared in 2012 (EI) (invited paper)
 12. Garcia Helen M., Abdulrahim Mujahid, Lind Rick, “Roll control for a micro air vehicle using active wing morphing”, *AIAA Guidance, Navigation, and Control Conference and Exhibit*, *AIAA 2003-5347*, 2003
 13. Smith, M. J. C., “Simulating moth wing aerodynamics: Towards the development of flapping-wing technology”, *AIAA Journal* 34, 1348-55, 1996
 14. Wang, Z. J., Birch, J. M., et al., “Unsteady forces and flows in low reynolds number hovering flight: Two-dimensional computations vs robotic wing experiments”, *Journal of Experimental Biology* 207, 449-60, 2004
 15. Ellington, C. P., “The aerodynamics of hovering insect flight: The quasi-steady analysis”, *Philosophical Transactions of the Royal Society of London, Series B* 305, 1-15, 1984a
 16. Shyy Wei, Lian Yongsheng, Tang Jian, Viieru Dragos, et al., “Aerodynamics of low reynolds number flyers”, *Cambridge Aerospace Series*, ISBN-13 978-0-521-88278-1, 2008
 17. Lighthill, M. J., “Introduction to the scaling of aerial locomotion”, in Pedley T. J. (Ed.), *Scale effects in animal locomotion* (New York, Academic), pp. 365-404, 1977
 18. Pennycuick, C. J., “Newton rules biology: A physical approach to biological problems” (New York, Oxford University Press), 1992
 19. Schmidt-Nielsen, K., “Scaling: Why is animal size so important?” (New York, Cambridge University Press), 1984
 20. Okamoto, M., Yasuda, K., and Azuma, A., “Aerodynamic characteristics of the wings and body of a dragonfly”, *Journal of Experimental Biology* 199, 281-94, 1996
 21. Sunada, S., Yasuda, T., Yasuda, K., and Kawachi, K., “Comparison of wing characteristics at an ultralow reynolds number”, *Journal of Aircraft* 39, 331-8, 2002
 22. Newman, B. G., Savage, S. B., et al., “Model test on a wing section of a dragonfly”, in Pedley T. J. (Ed.), *Scale effects in animal locomotion* (London, Academic), pp. 445-77, 1977
 23. Buckholz, R. H., “The functional role of wing corrugation in living system”, *Journal of Fluids Engineering* 108, 93-7, 1986
 24. Kesel, A. B., “Aerodynamic characteristics of dragonfly wing sections compared with technical airfoils”, *Journal of Experimental Biology* 203, 3125-35, 2000
 25. Kesel, A. B., “Biologisches Vorbild insektenflügel mehrkriterienoptimierung ultraleichtertragflächen”, in Nachtigall W. and Wisser A. (Eds.), *Biona-Report*, Vol. 12, pp. 107-17, 1998
 26. Jackson, P., “Jane's all the world's aircraft”, (Alexandria, VA, Jane's Information Group), 2001
 27. Tennekes, H., “The simple science of flight” (From insects to jumbo jets) (Boston, MIT Press), 1996
 28. Liu, T., “Comparative scaling of flapping- and fixed-wing flyers”, *AIAA Journal* 44, 24-33, 2006
 29. Kirkpatrick, S. J., “Scale effects on the stresses and safety factors in the wing bones of birds and bats”, *Journal of Experimental Biology* 190, 195-215, 1994
 30. Pennycuick, C. J., “Wingbeat frequency of birds in steady cruising flight: New data and improved predictions”, *Journal of Experimental Biology* 199, 1613-18, 1996
 31. Hill, A. V., “The dimensions of animals and their muscular dynamics”, *Science Progress* 38, 209-30, 1950
 32. Pennycuick, C. J., “Predicting wingbeat frequency and wavelength of birds”, *Journal of Experimental Biology* 150, 171-85, 1990
 33. Breitenstein Oliver, “Development of a flapping wing mechanism”, Semester Project Autonomous Systems Lab (ASL) and Swiss Federal Institute of Technology (ETH), Zurich, 2009
 34. Lehmann Fritz-Olaf, Pick Simon, “The aerodynamic benefit of wing-Wing interaction depends on stroke trajectory in flapping insect wings”, *The Journal of Experimental Biology* 210, 1362-1377, 2007
 35. Ennos A. Roland, “The kinematics and aerodynamics of the free flight of some dipterous”, *The Journal of Experimental Biology* 142, 49-85, 1989
 36. Weis-Fogh T., “Quick estimates of flight fitness in hovering animals, including novel mechanisms for lift production”, *The Journal of Experimental Biology* 59, 169-230, 1973
 37. Alexander, D. E., “Nature's Flyers”, Baltimore/London, Johns Hopkins University Press, 2002
 38. Guerrero Joel, “Numerical simulation of the unsteady aerodynamics of flapping flight”, Department of Civil, Environmental and Architectural Engineering, University of Genoa, A thesis submitted for the degree of Doctor of Philosophy, April 2009

39. Azuma, A., "The Biokinetics of Flying and Swimming", Tokyo, Springer-Verlag, 1992

40. Norberg U. M., Rayner J. M. V., "Ecological morphology and flight in bats (mammalia: Chiroptera): Wing adaptions, flight performance, foraging strategy and echolocation", Phil. Trans. R. Soc. Lond. B 316, 335-427, 1987

41. Hedenstrom A., Muijres F., von Busse R., Johansson L.C., Winter Y., Spedding G.R., "High-speed stereo DPIV measurements of bat wakes flying freely in a wind tunnel", Experiments in Fluids 46 (2009) 923-932, 2009

42. Muijres F. T. et al, "Leading-edge vortex improves lift in slow-flying bats", Science 319, 1250, 2008

43. Osborne, M. F. M., "Aerodynamics of flapping flight with application to insects", Journal of Experimental Biology 28, 221-45, 1951

44. Ellington C. P., Usherwood J.R., "Lift and drag characteristics of rotary and flapping wings", AIAA, 2001

45. Ansys fluent 12.0, Theory guide, April 2009

46. Busse von, R., "The trinity of energy conversion-kinematics, aerodynamics and energetics of lesser long-nosed bat (Leptonycteris yerbabuenae)", Ph.D. thesis, Humboldt University, Berlin, 2011

47. Tsai Bor-jang, Fu Yu-chun, "Design and aerodynamic analysis of a flapping-wing micro air vehicle", Aerospace Science and Technology, pp. 383-392, ISSN: 1270-9638 DOI:[10.1016/j.ast.2009.07.007](https://doi.org/10.1016/j.ast.2009.07.007), 2009.

48. von Busse Rhea, Hedenstro Anders, Winter York and Johansson L. Christoffer, "Kinematics and wing shape across flight speed in the bat, Leptonycteris yerbabuenae". Biology Open 1, pp. 1226-1238 doi:[10.1242/bio.20122964](https://doi.org/10.1242/bio.20122964), 2012.

49. Szmelter J., Zbikowski R., "Aerodynamic aspects of flapping wing micro air vehicles", ICAS-2000 Congress, pp. 134.1-8, 2000

ACKNOWLEDGMENTS

The authors would like to acknowledge and thank Prof. Frank Janser (FH Aachen UAS, Germany) for his valuable suggestions and guidance, Eugen Neu (Ph.D. scholar, FH Aachen UAS, Germany), for his assistance and support in computational analysis of the results and Smriti Singh for her significant help in reviewing the paper.

The Engineering Meetings Board has approved this paper for publication. It has successfully completed SAE's peer review process under the supervision of the session organizer. This process requires a minimum of three (3) reviews by industry experts.

All rights reserved. No part of this publication may be reproduced, stored in a retrieval system, or transmitted, in any form or by any means, electronic, mechanical, photocopying, recording, or otherwise, without the prior written permission of SAE.

ISSN 0148-7191

Positions and opinions advanced in this paper are those of the author(s) and not necessarily those of SAE. The author is solely responsible for the content of the paper.

SAE Customer Service:

Tel: 877-606-7323 (inside USA and Canada)

Tel: 724-776-4970 (outside USA)

Fax: 724-776-0790

Email: CustomerService@sae.org

SAE Web Address: <http://www.sae.org>

Printed in USA



CFD Modeling of Advanced Swirl Technique at Inlet-Runner for Diesel Engine

2015-26-0095

Published 01/14/2015

Bhagyada Dhingra

Vellore Institute of Technology

Sparsh Sharma

Moscow Institute of Physics & Technology

Kamalkishore Vora

ARAI

B Ashok

Vellore Institute of Technology

CITATION: Dhingra, B., Sharma, S., Vora, K., and Ashok, B., "CFD Modeling of Advanced Swirl Technique at Inlet-Runner for Diesel Engine," SAE Technical Paper 2015-26-0095, 2015, doi:10.4271/2015-26-0095.

Copyright © 2015 SAE International and Copyright © SAEINDIA

Abstract

This paper summarizes the research work incorporated in the exploration of the potential of swirling in CI Engine and designing of a new mechanism, particularly at inlet, to deliver it to improve the in-cylinder air characteristics to eventually improve mixing and combustion process to improve the engine performance.

The research is concentrated on the measures to be done on engine geometry so as to not only deliver advantage to any specific fuel. According to the CI combustion theory, better engine performance may be achieved with Higher Viscous Fuel by improving the in-cylinder air-fuel mixing by increasing the swirl (rotation of air view from top of the cylinder) and tumble (rotation of air view from front of the cylinder) of in-cylinder air inside the fuel-injected region. The proposed inlet component is embedded with airfoil and is suitably designed after being iterated from four steps. The deciding factors of shape and orientation of these airfoils are height, chord length and number of blades. The preliminary assessment of the proposed component is performed on a CFD code using incompressible Navier-Stokes with k-epsilon turbulence modeling. The 3D cold flow IC engine simulation is conducted on COSMOS and ANSYS Fluent. The validation of the results of in-cylinder airflow characteristics from simulations are compared with other related research works.

This paper is the first in series of our research on Diesel Engine. The experimental validation of the proposed component is currently going-on and would be presented in the next publication. The results show that the better mixing of fuel is achieved and the concentration of CO and Unburned Hydrocarbons is also reduced.

Introduction

The rate of depletion of petroleum based fuel due to automobiles is now driving the current generation of engineers and scientists to develop new techniques of extracting power from the fuel and enhancing the overall efficiency of existing techniques. Currently, the world has a huge number of automobiles on the road using Internal Combustion Engine (IC Engine). It is estimated by World Energy Forum in 2009 that the worldwide reserves of crude oil will be exhausted in less than 100 years [1]. Compression Ignition (CI) engines, more commonly known as diesel engines, can operate on conventional petroleum diesel fuel but also on neat vegetable oil [2,3], non-edible oil [4, 5, 6, 7], waste cooking oil [8] and biodiesel [9]. Moreover a CI engine can be operated on biodiesel [10], hence, biodiesel can be a potential alternative fuel to replace or supplement depleted crude oil. Many attempts had been made by researchers to utilize this advantage. Among them, Celikten et al [11] compared CI engine performance fuelled with diesel, rapeseed and soybean fuels. Bio-diesel experiences a reduction of maximum power and torque of 1.0 kW and 2.1 N.m respectively compared to diesel [11]. Additionally the fuel consumption of rapeseed and soybean were also reported to increase from diesel by about 29 g/kWh and 47 g/kWh, respectively. These problems are mainly due to the inferior chemical properties of biodiesel compared to the conventional diesel fuel. The viscosity and density of biodiesel were reported to be higher and volatility lower than diesel fuel [12,13,14] which lead to the incomplete combustion and this eventually produces lower engine performance and affects the durability of the engine [15,16]. Furthermore the emission of toxic gases like CO, HC, aldehydes, particles and black smokes are also reported to be lower, in comparison to burning diesel fuel, except NOX, which is higher. The researches in this area are focused to

improve the properties of biodiesel by using additives [17], pre-heating the fuel to level its viscosity to that of diesel [18] and adjusting the injection timing [19].

The current research is focused on the measures to be done on engine geometry so as to not only deliver advantage to any specific fuel. The most popular techniques employed to improve the combustion efficiency using HVF (Higher Viscous Fuel due to their higher viscosity compared to petroleum diesel fuel) are preheating HVF before injection [8, 20] and changing the injection timing [21]. According to the CI combustion theory, better engine performance may be achieved with HVF by improving the in-cylinder air-fuel mixing by increasing the swirl (rotation of air view from top of the cylinder) and tumble (rotation of air view from front of the cylinder) of in-cylinder air inside the fuel-injected region. Various methods have been used to improve the in-cylinder airflow in diesel engines such as: closing part of the intake port using a butterfly valve [22,23,24,25] modifying intake port/manifold geometry inserting shroud around the intake valve and modifying the piston bowl. Alternatively, in-cylinder airflow may be improved through the use of a guide vane.

One of the primary approaches to get the fuel entirely oxidized is to make it mix properly with the air is swirling or commonly known as turbulence. The more is the swirling of air-fuel mixture, the more breakdown of viscous fuel particle is. The breakdown of these heavy fuel particles occurs during the compression/combustion stroke. The concept of organized air flow is not new and was first found for carbureted engine using gasoline using gasoline by using rotating blades placed between carburetor and intake manifold to provide more air swirl for efficient air-fuel mixing [26]. Afterwards, atomizers and fuel molecule breaker were patented with different identities [14].

Instead of duplicating what has been done, this research explores the potential of swirling in CI Engine and designing of a new mechanism to deliver it to improve the in-cylinder air characteristics to eventually improve mixing and combustion process to improve the engine performance. The figure shown below shows the basic shape of airfoils which has been tested in present work.

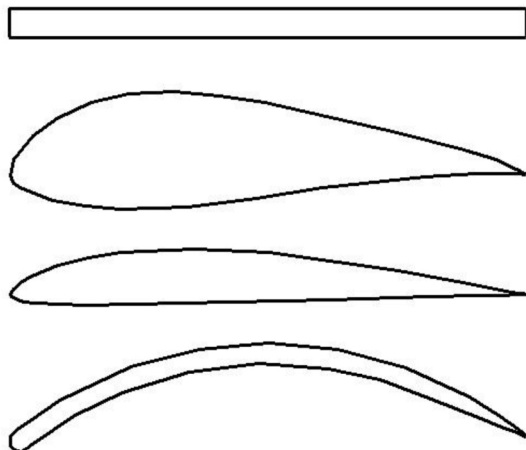


Figure 1. Different types of airfoil shortlisted for analysis

Swirl Generation during Induction

There are two broad tactics to create swirl during the induction stroke. In one, the flow is discharged tangentially toward the cylinder wall, where it is deflected sideways and downward in a swirling motion. In the other, the swirl is largely generated within the inlet port: the flow is forced to rotate about the valve axis before it enters the cylinder.

Governing Equations: COLD Flow Analysis

The three major equations used in the computational fluid dynamics problem are Continuity equation, Momentum equation (Navier-stokes equation) and Energy equation. For the generalized fluid flow problems mostly two equations are used. The first one is Continuity equation which fulfils the law of conservation of mass, thus a mass balance requirement posed in a mathematical form and the second one is Navier-stokes equation which fulfils the law of conservation of momentum. The Navier-stokes equations are vector hence they have separate set of equations for each coordinate direction. On the basis of control volume, the continuity equation is derived as follows:

$$\frac{\partial \rho}{\partial t} + \nabla \cdot (\rho U) = 0 \quad (1)$$

Where ρ is the fluid density and U is the three dimensional flow velocities in x, y and z directions. The Navier-stokes equation is based on the Newton's second law where the forces taken into account are body forces and surface forces on the control volume and is derived as follows:

$$\frac{\partial(\rho U)}{\partial t} + \nabla \cdot (\rho U \times U) = -\nabla p + \nabla \cdot \tau + S_M \quad (2)$$

In this equation p , τ and S_M are the fluid pressure, strain rate and momentum source, respectively. Since this problem is quite a complex thus the involvement of Energy equation in the calculations is inevitable. The rate of change of energy inside the fluid element which is equal to the combined net flux of heat into the element and the net rate of work done on the element due to the body and surface forces comprises the Energy equation which is further mathematically denoted as follows:

$$\frac{\partial(\rho h_{tot})}{\partial t} - \frac{\partial \rho}{\partial t} + \nabla \cdot (\rho U h_{tot}) = \nabla \cdot (\lambda \nabla T) + \nabla \cdot (U \cdot \tau) + U \cdot S_M \quad (3)$$

Where h_{tot} and λ represent the total enthalpy and thermal conductivity respectively of the fluid.

The engine simulation model is modelled conferring to the Kirloskar TAF-1 diesel engine coupled with a generator that operated at a constant speed of 1500 rpm. The technical specifications of the engine are listed in Table 2. SolidWorks 2014 is used to model the

essential drawings of the intake port, intake runner, intake valve, and cylinder volume. The dynamic analysis is carried out in ANSYS Fluent. The CFD simulation is carried out for only cold flow without combustion. At the boundaries i.e. at the intake as well as exhaust manifold, constant pressure conditions are given. Logarithmic law of wall unified with No-slip wall boundary condition is used. Moreover the simulation is dynamic and time dependent thus turbulence modeling comes into play.

Turbulence Modeling of the Swirling Flow

The swirl number is mathematically defined as follows:

$$SW = \frac{\int r v_\theta (\vec{v} \cdot \hat{n}) dS}{\bar{r} \int v_z (\vec{v} \cdot \hat{n}) dS} \quad (4)$$

where r is the radial coordinate (specifically, the radial distance from the axis of rotation), v_θ is the tangential velocity, \vec{v} is the velocity vector, \hat{n} a unit vector normal to the surface, S is the inlet or outlet.

For flows with weak to moderate swirl ($SW < 0.5$), both the RNG $k - \epsilon$ model and the realizable $k - \epsilon$ model yield appreciable improvements over the standard $k - \epsilon$ model. For highly swirling flows ($SW > 0.5$), the RNG $k - \epsilon$ model is strongly recommended. The effects of strong turbulence anisotropy can be modeled rigorously only by the second-moment closure adopted in the RNG $k - \epsilon$ model

In this study RNG $k - \epsilon$ model is used. "k" is the turbulence kinetic energy and is defined as the variance of the fluctuations in velocity and "ε" is the turbulence eddy dissipation and has dimensions of k per unit time. The TKE equation after few simplifications is as follows:

$$\frac{\partial k}{\partial t} + u_j \frac{\partial k}{\partial x_j} = \tau_{tij} \frac{\partial u_i}{\partial x_j} - \epsilon + \frac{\partial}{\partial x_j} \left[V + \frac{v_t}{\sigma_k} \frac{\partial k}{\partial x_j} \right] \quad (5)$$

$$\tau_{tij} = -\overline{u_i u_j} = 2v_t S_{ij} - \frac{2}{3} k \delta_{ij} \quad (6)$$

The first term on the RHS is the production of 'k', the second term (ϵ) is the specific dissipation per unit mass. The last terms describe the transport of 'k' by molecular and turbulent diffusion. This model is best suited for flows with high Reynolds number where turbulence is almost isotropic. The scale elimination procedure in RNG theory results in a differential equation for turbulent viscosity:

$$d \left(\frac{\rho^2 k}{\sqrt{\epsilon} \mu} \right) = 1.72 \frac{\hat{v}}{\sqrt{\hat{v}^3 - 1 + C_v}} d\hat{v} \quad (7)$$

$$\hat{v} = \mu_{eff}/\mu$$

$$C_v \approx 100$$

The problem here is axisymmetric with respect to geometry and flow conditions and includes swirl or rotation. In this case, the flow can be

modelled as 2D for initial purpose so as to save the time (i.e., solve the axisymmetric problem) and include the prediction of the circumferential (or swirl) velocity. It is important to note that while the assumption of axisymmetric implies that there are no circumferential gradients in the flow, there may still be non-zero swirl velocities as shown in the figure:

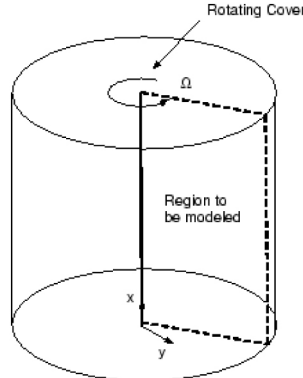


Figure 2. In-cylinder picture showing the region needed to be modeled

Dynamic Meshing for Piston Movement

The to and fro motion of piston is modeled using the technique known as Dynamic mesh. It allows the movement of the boundaries of a cell zone relative to other boundaries of the zone, and to adjust the mesh accordingly. The boundaries can move rigidly with respect to each other (i.e., linear or rotational motion), and/or deform. The relative motion of stationary (cylinder) and moving (piston) components gives rise to transient interactions.

Mesh Update Method

As per the availability of mesh motion methods in ANSYS Fluent, Spring-Based Smoothing and Dynamic Layering Method are chosen which are further explained in subsequent section.

Spring-Based Smoothing

In the spring-based smoothing method, the edges between any two mesh nodes are idealized as a network of interconnected springs. The initial spacing's of the edges before any boundary motion constitute the equilibrium state of the mesh. A displacement at a given boundary node will generate a force proportional to the displacement along all the springs connected to the node. Using Hooke's Law, the force on a mesh node can be written as [45]:

$$\vec{F}_i = \sum_j^{n_i} k_{ij} (\Delta \vec{x}_j - \Delta \vec{x}_i) \quad (8)$$

where $\Delta \vec{x}_i$ and $\Delta \vec{x}_j$ are the displacements of node i and its neighbor j , n_i is the number of neighboring nodes connected to node i , and k_{ij} is the spring constant (or stiffness) between node i and its neighbor j . The spring constant for the edge connecting nodes i and j is defined as

$$k_{ij} = \frac{1}{\sqrt{|\vec{x}_i - \vec{x}_j|}} \quad (9)$$

Dynamic Layering Method

In prismatic mesh zones, dynamic layering method adds or removes layers of cells adjacent to a moving boundary, based on the height of the layer adjacent to the moving surface. The dynamic mesh model in ANSYS FLUENT allows you to specify an ideal layer height on each moving boundary.

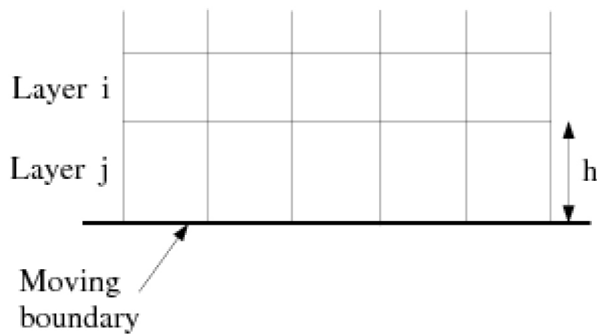


Figure 3. Dynamic layering at the moving boundary layer (piston-cylinder wall)

If the cells in layer j are expanding, the cell heights are allowed to increase until

$$h_{\min} > (1 + a_s)h_{\text{ideal}} \quad (10)$$

Here h_{\min} is the minimum cell height of cell layer j , h_{ideal} is the ideal cell height, and a_s is the layer split factor.

If the cells in layer j are being compressed, they can be compressed until

$$h_{\min} < a_c h_{\text{ideal}} \quad (11)$$

where a_c is the layer collapse factor. When this condition is met, the compressed layer of cells is merged into the layer of cells above the compressed layer; i.e., the cells in layer j are merged with those in layer i .

Implicit Update Settings

For such applications, having the mesh motion updated within the time step based on the converging flow solution results in a stronger coupling between the flow solution and the mesh motion, and leads to a more robust solver run. Implicit mesh updating allows you to run simulations that otherwise could not be solved or would require an unreasonably small time step. The relaxation of the displacements is defined by the following equation [45]:

$$x_k = \omega(x_{\text{computed},k}) + (1 - \omega)x_{k-1} \quad (12)$$

Where x_k is the node position at iteration k (within a time step), $x_{\text{computed},k}$ is the computed node position (based on the flow field), and ω is the motion relaxation.

The simulation goes projected when the geometry gets the required set of physical parameters associated with the operational conditions. In preceding sections, it is decided to go with k- ϵ Turbulence modelling with dynamic meshing supported by spring based smoothing and dynamic layering.

Boundary Conditions

This section describes the associated boundary conditions with the suction stroke in CI engine. There is no turbocharging linked with the in-take stroke. The following figure shows all the attached boundary conditions to every important component.

The simulation goes projected when the geometry gets the required set of physical parameters associated with the operational conditions. In preceding sections, it is decided to go with k- ϵ Turbulence modeling with dynamic meshing supported by spring based smoothing and dynamic layering.

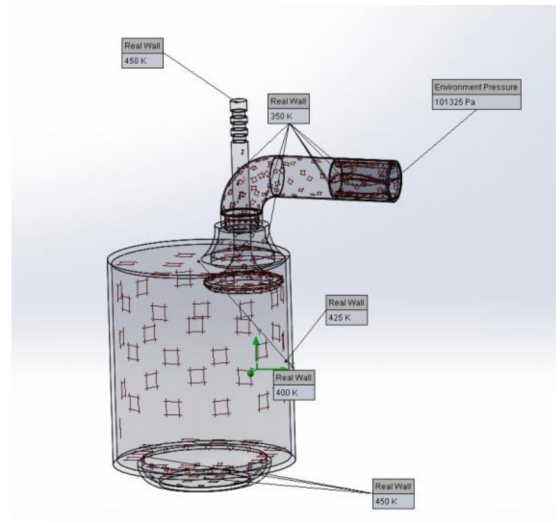


Figure 4. Engine geometry showing all the boundary conditions attached

The following [Table 1](#) tabulates all the boundary conditions attached to its respective component.

Table 1. Boundary conditions attached to their significant component

Component	Boundary Condition
Opening of inlet runner	P=101325 Pa; T= 300K (Environmental pressure)
Inlet runner pipe	T=350K (Real wall)
Valve	T=450K (Real wall)
Top surface of the cylinder	T=400K (Real wall)
In-cylinder wall	T=425K (Real wall)
Bottom of the cylinder and top of the piston	T=450K (Real wall)

Simulation Results and Discussion

A complete parametric study of four different types of blade shape incorporated in the component is done computationally in this chapter. Parametric study is performed with the component maintaining the constant engine geometry throughout the analysis for four different configurations namely S1 to S4.

The method of testing adopted for this project is one of learning from the results of each shape tested, and implementing appropriate changes in the subsequent blade shape. The best configuration is then chosen after analyzing computational result and comparing various plots for in-cylinder velocity and vorticity.

As for preparing the simulation model, SolidWorks 2014 was utilized to draw the four different blade shape design and S1 to S4 configuration for Advanced Swirl Device (ASD). The best design is then chosen by comparing the results obtained by CFD analysis.

The for k- ϵ turbulence modeling brought the following plots. It can be construed from the figure shown below that the velocity of the fluid at the cylinder wall is apparently negligible as compared to the velocity in the core of cylinder. This evidences the problem of formation of thin wall of charge inside the cylinder in CI engine.

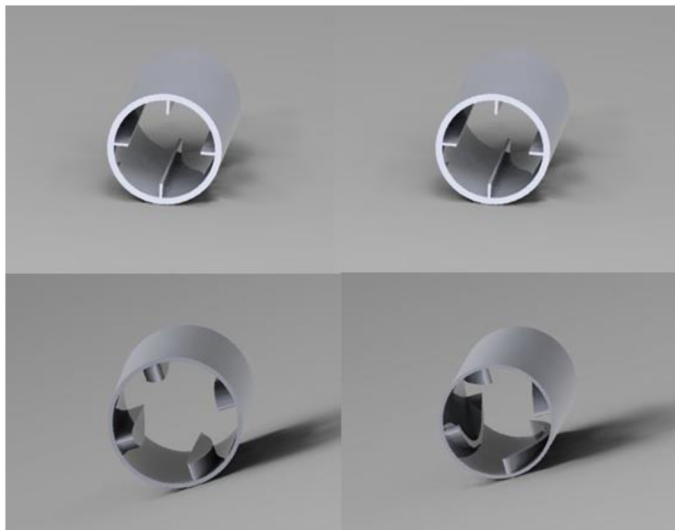


Figure 5. ASD-S1 to S4 (from left to right)

Additionally, vorticity plot also shows a level of turbulence (disturbance) directly beneath the port which fades out when moving away from the axis in radial direction. The blue color depicts the zero magnitude of swirl parallel to the cylinder head plane as shown in [figure 6](#).

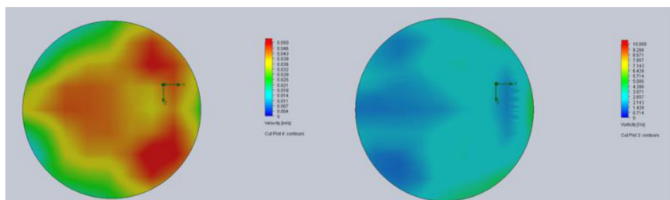


Figure 6. Cut plot showing velocity (left) and vorticity (right) distribution in baseline configuration

In the [figure 7](#), a comparison of velocity among all the proposed ASDs is shown. The in-cylinder velocity in S1 and S3 is relatively less when compared with that of S2 and S4. The more the green color a plot has the less the swirl it has and adhering to which configurations S1 and S3 simply draw out from the further comparison. Now moving towards the left ones, S4 delivers high in-cylinder velocity at almost every point.

Nevertheless S4 has a static region in the right side of the cylinder, S2 has certainly very low velocity in the core of the cylinder.

Next illustration ([figure 8](#)) shows the vorticity cut plot. The circular motion along the vertical axis or simply swirl is inferred from this plot. Configuration S1 delivers mixed response whereas S2 and S4, as expected, distribute more swirl inside the cylinder. Performance of S3 is dramatically poor in this context, the flow remain irrotational all the time. The more the rotational flow near the walls, the less the formation of fluid film there; S4 has more vorticity vectors at every visible location inside the cylinder as compared to others.

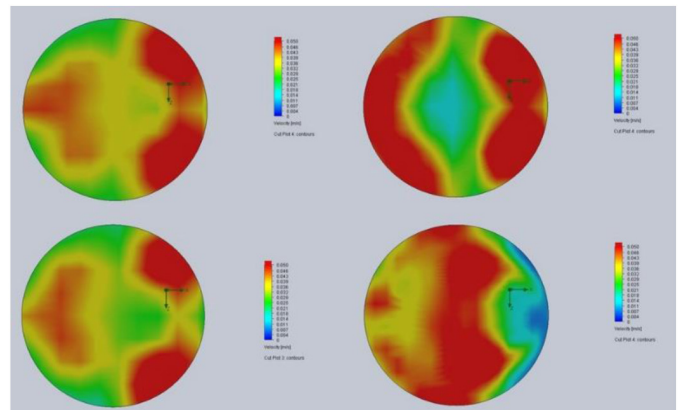


Figure 7. Cut plot showing velocity distribution in S1-S4 (clockwise from top left) configurations

Adding up the results from all the cut plots, it is inferred that S2 and S4 are the best possible designs for ASD, but to move on for further iteration process it is suggested to select the best so that advance design changes can be introduced into the selected design. A thorough analysis of the plots suggest a draw between S2 and S4 whereas [figure 7](#) and [8](#) characterize the drawbacks in S2 thus marking S4 as the best suited ASD design.

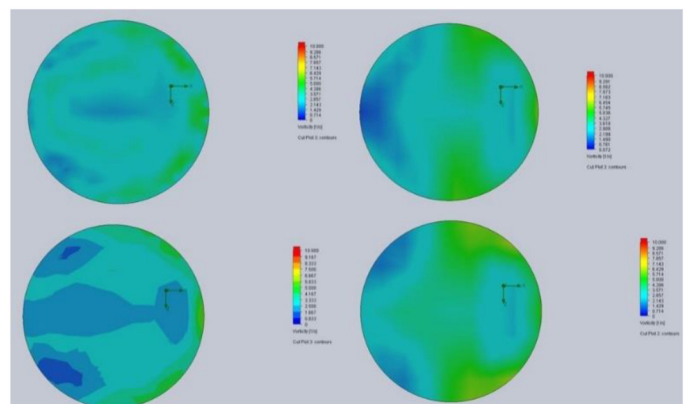
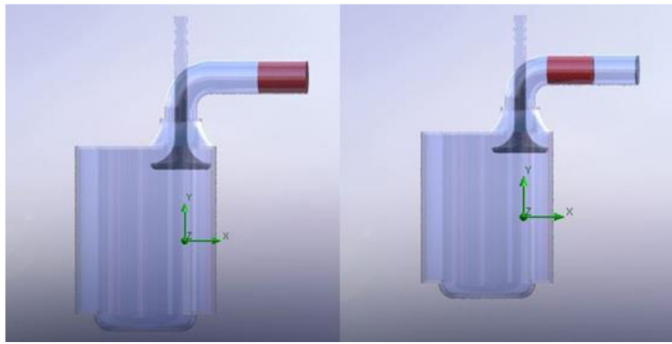


Figure 8. Cut plot showing vorticity distribution in S1-S4 (clockwise from top left) configurations

The overhead discussion simply suggest that configuration S4 is best among all the proposed designs, thus the usage of a cambered airfoil in the inlet runner can be considered fruitful in terms of increasing in-cylinder velocity and swirl resulting in less emission.

Since this is a progressive iteration process, S4 moves on the next iteration process and will be tested with next design optimization.

After being decided upon the shape, the designing process of ASD arrives at phase-2. The positioning of the device is considered the second important parameter. Parametric study is carried out with the component placed at two different positions namely L1 and L2 as shown in [figure.9](#).



[Figure 9. ASD-L1 \(left\) and ASD-L2 \(right\)](#)

The cut plot shown in [figure.10](#) shows the difference between velocity distributions inside the cylinder delivered by L1 (left) and L2 (right). In configuration L1, the particle moves somewhat slower inside the cylinder, the yellow region near the ports and around the walls proves this.

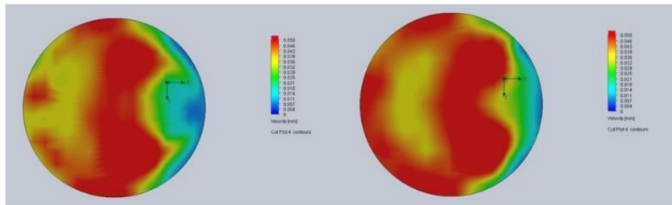


[Figure 10. Cut plot showing velocity distribution in L1 \(left\) and L2 \(right\) configurations](#)

Looking at L2 configuration, the red portion is more than any other color. The velocity near the axis of the cylinder is also very high in this case. On the right side of the cylinder, blue color is visible which shows the area of high tumble, this is caused due to usage of conventional valve in the analysis.

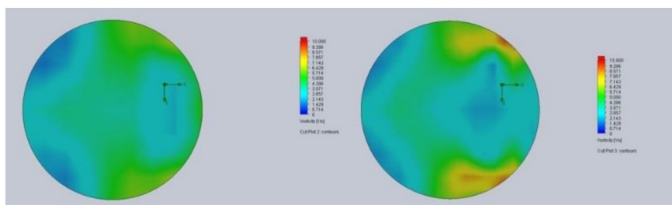


[Figure 11. Cut plot showing vorticity distribution in L1 \(left\) and L2 \(right\) configurations](#)

[Figure.11](#) shows the vorticity plot for both the configurations. The swirl intensity is high in L2 configuration at every place. On the walls where velocity seems to less in previous graph, vorticity plot evidences the presence of high swirl at those positions. In L1 the swirl is critically less the left side of the cylinder whereas in L2 the red and yellow color confirms the high swirl.

From above interpretation, ASD-S4-L2 comes out to be the best and can be moved on the next the iteration phase.

Till now S4 shape with L2 positioning is confirmed by the robust computational analysis. This chapter deals with the optimization of the component for number of blades. A parametric study is performed with the component maintaining the constant engine geometry throughout the analysis. Three different ASDs with different number of blades have been modeled, in SolidWorks 2014, namely B1, B2, and B3.

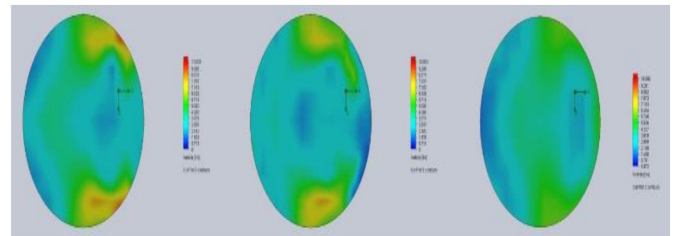


[Figure 12. Cut plot showing velocity distribution in B1, B2, and B3 \(from left to right\)](#)

The [figure.12](#) illustrates the velocity distribution inside the cylinder. All the three configuration differ from each other. The plot on the extreme right (eight blade configuration) has almost zero velocity around the wall of the cylinder. The two red spots around the central axis show high velocity swirls in the center but due to the presence of more blue and green color it stands last in the comparison. Coming to the configuration B2 (six blades), the velocity around the wall on the right side is pretty low but in the core of cylinder the presence of more red color is quite an evidence of high velocity vectors

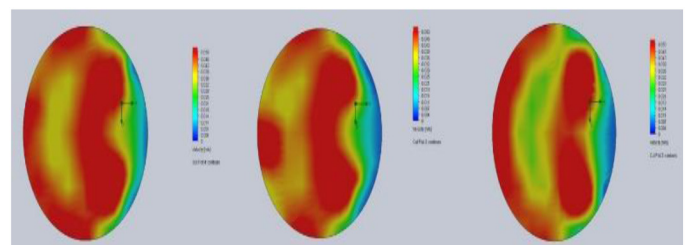


[Figure 13. Cut plot showing vorticity distribution in B1, B2, and B3 \(from left to right\)](#)

With the most of red color inside the cylinder, configuration with four blades can be considered as the best in terms of velocity distribution. The little yellow spot near the left wall shows some static region but overall it has better performance capabilities.

Now comes to the vorticity plot. This plot also favors the coin to B1. The high pressure swirl is present around the wall of B1. B2 also has good turbulence relative to B1. Upon looking B3, there is no sign of high swirl.

From above interpretation, ASD-S4-L2-B1 comes out to be the best and can be moved on the next the iteration phase.

This section is the last in this iteration process, counts the parametric study of three different configurations of ASD with four blades but of different heights namely H1, H2, and H3. The study is performed with components maintaining the constant engine geometry throughout the analysis.

The next plot is the velocity distribution inside the cylinder of all the three configurations having blades with different height as shown in figure 14. The picture in the extreme right is having blade of 4.5mm length. It is previously mentioned that these blades will impart obstruction to the air flow. Furthermore, the presence of more green and yellow color in H3 prove the presence of static dead fluid zone which is not good for combustion. Now coming to H2 (picture in the middle), the velocity vector is somewhat increased relatively H1, yet the presence of more yellow and red color in this configuration prove that increasing the length of blade is definitely increasing the obstruction to the incoming air. Now moving to H1 (extreme left) which has blade height of 2.5mm length. The velocity near the wall and around the central axis is comparatively high compared to every other configuration.

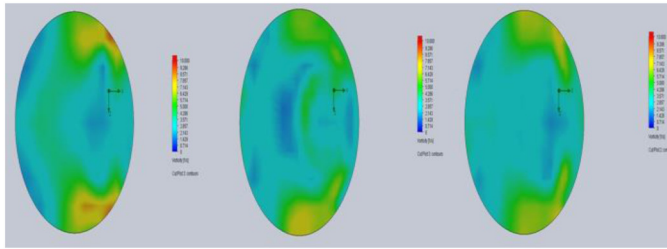


Figure 14. Cut plot showing vorticity distribution in H1, H2, and H3 (from left to right)

The final plot in the series of this long iteration process is the vorticity plot accommodating H1, H2, and H3 as shown in figure 15. Looking at the extreme right, H3 configuration, the vorticity around the wall is observed which diminishes when moving in to the central axis. Two dead zones are clearly visible. H2 delivers a surprisingly high vortical flow with yellow portion motivating the presence of swirls. Finally coming to H1, i.e. 2.5mm long blades, the vortical flow is strongest in this configuration with least concentration of dead fluid zones. The red portion on the right side of the cylinder wall is a great indication of high velocity swirl.

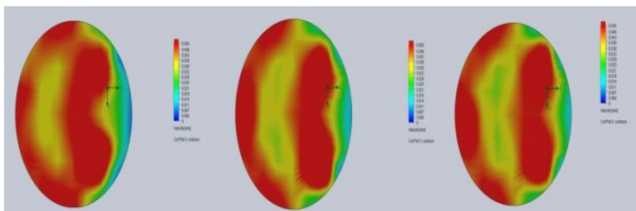


Figure 15. Cut plot showing vorticity distribution in H1, H2, and H3 (from left to right)

From above interpretation, ASD-S4-L2-B1 comes out to be the best and can be moved on the next phase of this project which is prototyping and experimental tests on engine bed.

Experimental Results and Discussion

This section is certainly the most important chapter of this paper. It includes the prototyping of Advanced Swirl Device and its installation, commissioning and run of the engine. Substantial development of the engine test facility was necessary before testing could begin.

After being iterated in long designing process ASD has finally taken its shape. The CAD model is prepared in SolidWorks 2014 and has been scaled up for the purpose for being tested on the available facility. The manufacturing process incorporated in manufacturing ASD is also mentioned in this chapter.

The engine available at VIT University is a Kirloskar TAF-1 diesel engine used for agricultural application which is a constant speed of 1500 rpm. Full specification of this engine and installation of ASD at the inlet runner is elaborated in this chapter.

The final section deals with the results and validates the computational results obtained from CFD analysis.



Figure 16. Manufactured blades (left) according to S4-B1-H1 configuration and the final ASD (right) with blades embedded inside the cylindrical pipe

The final ASD as shown in figure 16 has been manufactured using CNC

The engine simulation model is modelled conferring to the Kirloskar TAF-1 diesel engine that operated at a constant speed of 1500 rpm is coupled with a eddy current dynamometer. The technical specifications of the engine are listed in Table 2. SolidWorks 2014 is used to model the essential drawings of the intake port, intake runner, intake valve, and cylinder volume.

The analysis is done for 5 load variations namely 20%, 40%, 60%, 80%, and 100%; with and without ASD.



Figure 17. Kirloskar TAF-1 Diesel Engine

The engine test is made possible not only because of engine but also the auxiliaries like electronic display board which shows engine speed in rpm, data acquisition system recording every bit, fuel tank holding enough diesel fuel for the test, gas analyzer for analyzing the emission constituents, and dynamometer. Schematic diagram of the experimental set up is depicted in [figure 18](#).

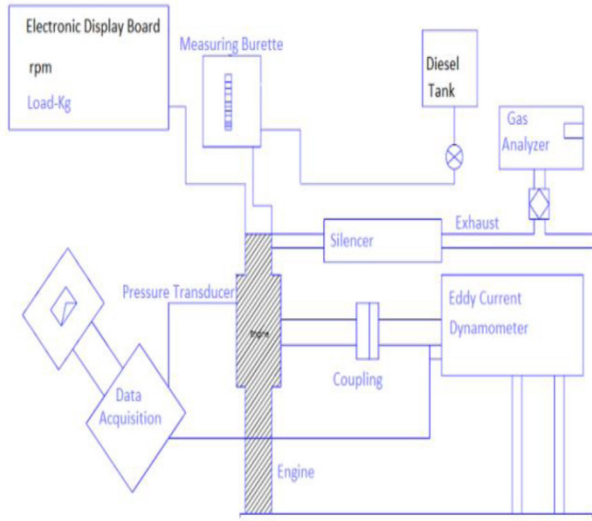


[Figure 18. Overall experimental set-up](#)

[Table 2. Engine specifications](#)

Parameter	Value
No. of Cylinders	1
Bore * Stroke	87.5 x 110mm
Cubic Capacity	0.662 ltr
Compression Ratio	17.5:1
Rated Output	4.41 KW
Rated Speed :	1500 rpm (Constant Speed)
Specific Fuel Capacity (SFC)	195 gm/hp-hr
Fuel Tank Capacity	6.5 ltr
Engine Weight (dry)	163 kg
Starting :	Hand start

The following table tabulates engine specifications in a broad way.

When the engine speed is kept constant, the performance of a diesel engine is mainly dictated by the quantities of diesel fuel injected. Usually, the specific fuel consumption decreases while the exhaust temperature increases with the increase in engine power, and NOx and CO2 emissions increase with the increased addition of the diesel

fuel. The same phenomena is observed here but a variation in the concentration of CO2 and NOx in both the engine configuration is observed.

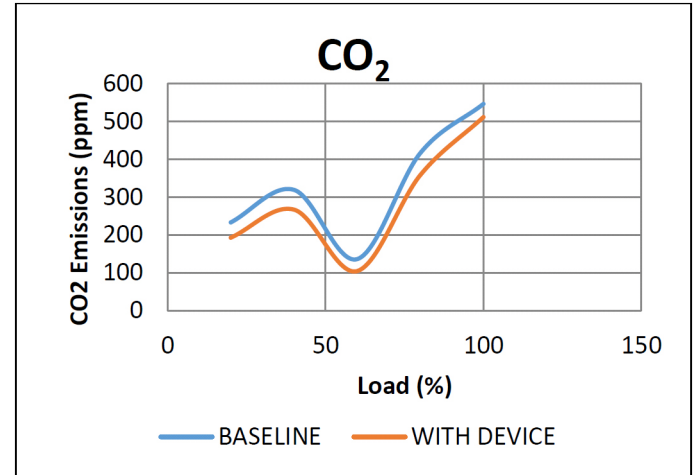


[Figure 19. CO2 emissions vs load](#)

Both the graphs show no deviation to each other. At 20% load the baseline engine run produces 233ppm CO2 whereas run with ASD produces only 193ppm which is 40ppm less CO2 emissions at minimal load. At 40% load, ASD engine run emits 50ppm less CO2. This trend is dominant for all the load values and on an average engine with ASD emits 45ppm less CO2 than an engine without ASD.

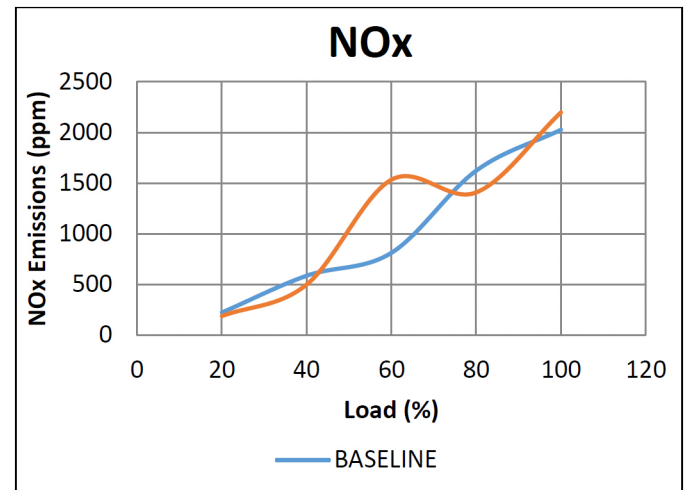


[Figure 20. NOx emissions vs load](#)

Since the NOx formation is more complex than any other pollutant so are its measures. At nominal load of 20%, instead of a drop in NOx emissions, an unexpected rise of 35ppm is observed which could be estimated due to more mixing inside the cylinder. At 40% load the emissions get lower in ASD engine whereas the baseline engine keep following the same trend. It can be simply inferred from the [figure 20](#) that NOx emission increases in engine with ASD which could a possible outcome of more mixing. So it is advisable for future work if catalytic converter can be incorporated in the research work for further development of this new idea.

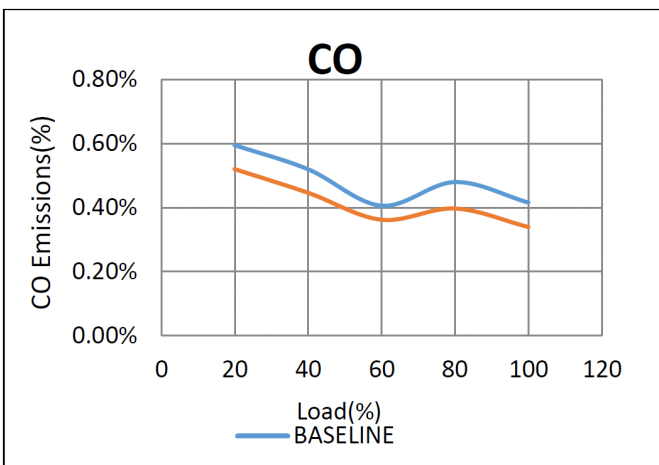


Figure 21. CO emissions vs load

The results obtained for CO and unburned hydrocarbons, the ASD seem advantageous. With the increment in load from 20% to full load condition reduction of 0.05% CO to 0.07% CO emissions are observed with the usage of ASD.

From initial load variation to the final load, a drop of HC emissions is observed in the range of 50 ppm to 200 ppm with the usage of ASD.

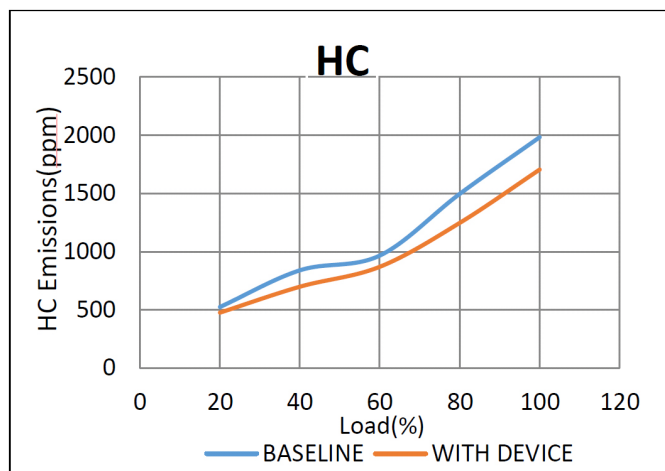


Figure 22. HC emissions vs load

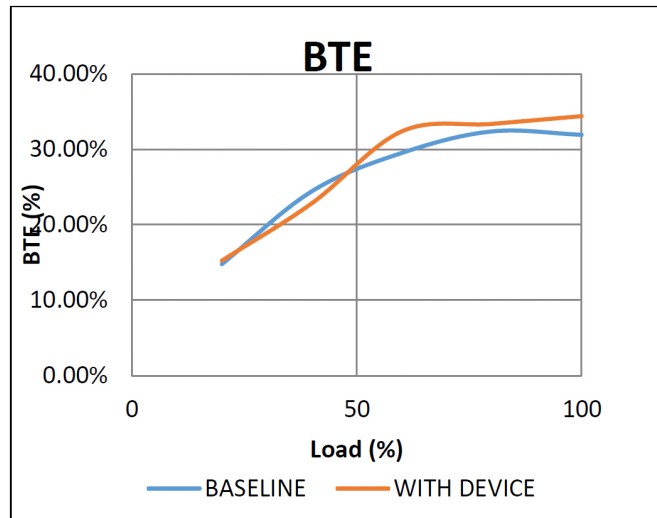


Figure 23. Brake Thermal Efficiency (BTE)

Concluding remark in favor of ASD is evidently given by this positive variation in BTE. At initial 20% load, there is no difference observed in efficiencies of both the configurations.

Till 50% load conditions, baseline performs better in terms of efficiency but after 50% the configuration with ASD topples up everything in favor of this new invention. An overall rise of 3.12% is calculated, which means using ASD increases the BTE by 3%.

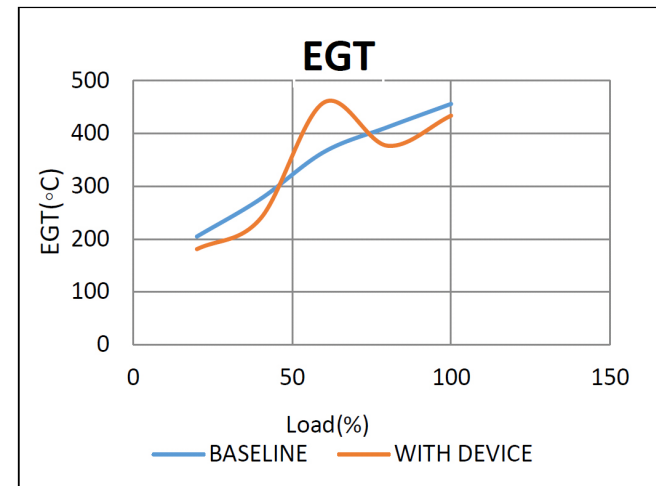


Figure 24. Exhaust Gas Temperature (EGT)

Certainly the reason for trivial performance of ASD for NOx emissions could be explained with the help of figure 24. A very oscillating data has been recorded for EGT. Between the intervals of 40% load to 75% load, engine with ASD produces higher temperature exhaust whereas the baseline engine shows a linear curve for all the ranges of loads. Beyond 80% load conditions, ASD lowers down the exhaust gas temperature by 5%.

Summary & Conclusions

Advanced Swirl Devices (ASDs) were tested by performing a rigorous design and analyses process consisting of both CFD simulations and experimental tests on an engine bed. This encompassed a wide range of boundary conditions, engine speeds and loads. And provided a suitable basis upon which to compare the emissions performance of each ASD.

Substantial variances in the trend of CO₂, NOx, CO and unburned Hydrocarbons between different mode tests.

The figure shown below depicts the advantage ASD is delivering in terms of enhancing swirl and mixing of fuel-air particles. The more red color is visible in ASD configuration which evidences more turbulence and swirl inside the chamber.

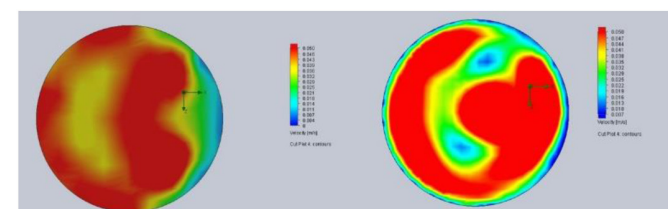


Figure 25. Cut plot showing velocity comparison between baseline (left) and ASD-S4-L2-B1-H1

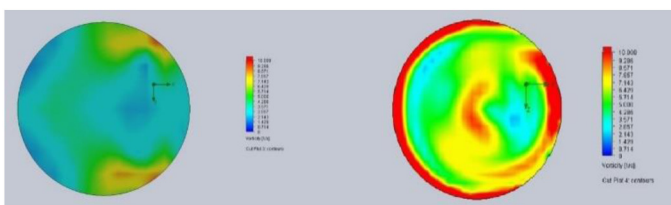


Figure 26. Cut plot showing vorticity comparison between baseline (left) and ASD-S4-L2-B1-H1

ASD-S4-L2-B1-H1 has been prototyped and is tested on the engine bed. The engine ran twice; one with the device and one without device. The fuel used is diesel without pre-heating. The exhaust gas analyzer analyzed the exhaust at every load and it is evidently recorded that the application of ASD at the inlet reduces CO₂, CO, Unburned HCs. This is due to the proper mixing of air-fuel particles because as expected ASD has imparted high velocity vortical flow into the cylinder.

A drop in the range of 50-200 ppm is observed in HC emissions, furthermore a reduction of 0.05% CO is also observed. While moving towards CO₂ a descent of 50ppm is achieved.

Brake thermal efficiency is surprisingly increased by 3% which needs to be validated with more robust engine tests in future.

References

1. Sharma, Y.C. and Singh B., Development of biodiesel: Current scenario. *Renewable and Sustainable Energy Reviews*, 2009. 13(6-7): p. 1646-1651.
2. Lim, S. and Lee K.T., Implementation of biofuels in Malaysian transportation sector towards sustainable development: A case study of international cooperation between Malaysia and Japan. *Renewable and Sustainable Energy Reviews*, 2012. 16(4): p. 1790-1800.
3. Bari, S., Yu C., and Lim T., Performance deterioration and durability issues while running a diesel engine with crude palm oil. *Proceedings of the Institution of Mechanical Engineers, Part D: Journal of Automobile Engineering*, 2002. 216(9): p. 785-792.
4. Russo, D., et al., State of the art of biofuels from pure plant oil. *Renewable and Sustainable Energy Reviews*, 2012. 16(6): p. 4056-4070.
5. Atabani, A.E., et al., A comprehensive review on biodiesel as an alternative energy resource and its characteristics. *Renewable and Sustainable Energy Reviews*, 2012. 16(4): p. 2070-2093.
6. Ayhan, D., Use of algae as biofuel sources. *Energy Conversion and Management*, 2010. 51(12): p. 2738-2749.
7. Demirbas, A. and Fatih Demirbas M., Importance of algae oil as a source of biodiesel. *Energy Conversion and Management*, 2011. 52(1): p. 163-170.
8. Bari, S., Lim T.H., and Yu C.W., Effects of preheating of crude palm oil (CPO) on injection system, performance and emission of a diesel engine. *Renewable Energy*, 2002. 27(3): p. 339-351.
9. Kumar, D.J. and Binnal P., Performance evaluation of a single cylinder diesel engine fueled with biodiesel produced from pumpkin oil. *Journal of Scientific & Industrial Research*, 2012. 71: p. 75-78.
10. Murugesan, A., et al., o as an alternative fuel for diesel engines-A review. *Renewable and Sustainable Energy Reviews*, 2009. 13(3): p. 653-662.
11. Çelikten, İ., Koca A., and Ali Arslan M., Comparison of performance and emissions of diesel fuel, rapeseed and soybean oil methyl esters injected at different pressures. *Renewable Energy*, 2010. 35(4): p. 814-820.
12. Agarwal, A.K., (2007). Biofuels (alcohols and biodiesel) applications as fuels for internal combustion engines. *Progress in Energy and Combustion Science* 33(3), 233-271.
13. Candeia, R.A., Silva, M.C.D., Carvalho Filho, J.R., Brasilino, M.G.A., Bicudo, T.C., Santos, I.M.G., Souza, A.G., (2009). Influence of soybean biodiesel content on basic properties of biodiesel-diesel blends. *Fuel* 88(4), 738-743.
14. Jaichandar, S., Annamalai, K., Effects of open combustion chamber geometries on the performance of pongamia biodiesel in a DI diesel engine. *Fuel* (0).
15. Bari, S., (2004). Investigation into the deteriorated performance of diesel engine after prolonged use of vegetable oil, ASME 2004 Internal Combustion Engine Division Fall Technical Conference ASME, Long Beach, California, USA.
16. Bari, S., Yu, C., Lim, T., (2002b). Filter clogging and power loss issues while running a diesel engine with waste cooking oil. *Proceedings of the Institution of Mechanical Engineers, Part D: Journal of Automobile Engineering* 216(12), 993-1001.
17. Moser, B.R., (2008). Influence of Blending Canola, Palm, Soybean, and Sunflower Oil Methyl Esters on Fuel Properties of Biodiesel†. *Energy & Fuels* 22(6), 4301-4306.
18. Pugazhvadivu, M., Jeyachandran, K., (2005). Investigations on the performance and exhaust emissions of a diesel engine using preheated waste frying oil as fuel. *Renewable Energy* 30(14), 2189-2202.
19. Ye, P., Boehman, A.L., (2012). An investigation of the impact of injection strategy and biodiesel on engine NOx and particulate matter emissions with a common-rail turbocharged DI diesel engine. *Fuel* 97(0), 476-488.
20. Agarwal, D. and Agarwal A.K., Performance and emissions characteristics of Jatropha oil (preheated and blends) in a direct injection compression ignition engine. *Applied Thermal Engineering*, 2007. 27(13): p. 2314-2323.
21. Bari, S., Yu C., and Lim T., Effect of fuel injection timing with waste cooking oil as a fuel in a direct injection diesel engine. *Proceedings of the Institution of Mechanical Engineers, Part D: Journal of Automobile Engineering*, 2004. 218(1): p. 93-104.
22. Reeves, M., et al., Barrel swirl breakdown in sparkignition engines: insights from particle image velocimetry measurements. *Proceedings of the Institution of Mechanical Engineers, Part D: Journal of Automobile Engineering*, 1999. 213(6): p. 595-609.
23. Rizalman Mamat, et al. Effect of Air Intake Pressure Drop on Performance and Emissions of a Diesel Engine Operating with Biodiesel and Ultra Low Sulphur Diesel (ULSD). In International Conference on Renewable Energy and Power Quality (ICREPQ'09). 2009. Valencia, Spain.

24. Benajes J., et al., The effect of swirl on combustion and exhaust emissions in heavy-duty diesel engines. Proceedings of the Institution of Mechanical Engineers, Part D: Journal of Automobile Engineering, 2004. 218(10): p. 1141-1148.
25. Kim, K., et al., Investigation of the Swirl Effect on Diffusion Flame in a Direct-Injection (DI) Diesel Engine Using Image Processing Technology. Energy & Fuels, 2008. 22(6): p. 3687-3694.
26. Saad Idris, Bari, S., (2011). Effects of Guide Vane Swirl and Tumble Device (GVSTD) to the Air Flow of Naturally Aspirated CI Engine, in: Prof. Ali Mohammad (Ed.), International Conference on Mechanical Engineering 2011 (ICME2011). Progressive Printers Pvt. Ltd., Dhaka, Bangladesh.

Contact

Bhagyada Dhingra
Fiat-Chrysler Automotive pvt Ltd.
bhagyada.dhingra@fcagroup.com

Sparsh Sharma
Moscow Institute of Physics & Technology
sssparsh14@gmail.com

The Engineering Meetings Board has approved this paper for publication. It has successfully completed SAE's peer review process under the supervision of the session organizer. The process requires a minimum of three (3) reviews by industry experts.

All rights reserved. No part of this publication may be reproduced, stored in a retrieval system, or transmitted, in any form or by any means, electronic, mechanical, photocopying, recording, or otherwise, without the prior written permission of SAE International.

Positions and opinions advanced in this paper are those of the author(s) and not necessarily those of SAE International. The author is solely responsible for the content of the paper.

ISSN 0148-7191

<http://papers.sae.org/2015-26-0095>